DISSERTATION

COLORADO STATE UNIV'S THESIS TEMPLATE

Submitted by

Matthew Gregory Hogan

Department of Physics

In partial fulfillment of the requirements

For the Degree of Doctor of Philosophy

Colorado State University

Fort Collins, Colorado

Summer 2019

Doctoral Committee:

Advisor: Walter Toki
Co-Advisor: Robert Wilson

Norman Buchanan
Wen Zhou

Copyright by Matthew Gregory Hogan 2019

All Rights Reserved

ABSTRACT

COLORADO STATE UNIV'S THESIS TEMPLATE

This document aims to get you started typesetting your thesis or dissertation in LaTeX.

ACKNOWLEDGEMENTS

I would like to thank the Elliott Forney for making a publicly accessible LaTeX template

TABLE OF CONTENTS

LIST OF TABLES

LIST OF FIGURES

Chapter 1

Introduction

Chose trop vue n'est chère tenue

A thing too much seen is little prized

French proverb

1.1 Introduction to Neutrinos

The history of the neutrino can be traced back to electron energy spectrum observed in neutron β-decay. While measurements of α- and γ-decay of atomic nuclei showed discrete spectral lines, the electron (β particle) exhibited a continuous energy spectrum. Experimentally, there were two observed particles in each decay process and classical physics dictated that the outgoing daughter particles should have discrete energies. The fact that the β-decay spectrum was not this way posed a fundamental problem for physicists in the mid-1910s and later, was energy conserved? Two solutions were postulated: either the "energy conservation law is only valid statistically in such a process [...] or an additional undetectable new particle [...] carrying away the additional energy and spin [...] is emitted [32]." The latter solution was supported by Wolfgang Pauli in a letter dated 4 December 1930 to a group of physicists meeting in Tübingen, modern Germany, where he first proposed the neutrino[1]. Pauli's solution also predicted that the undetected neutrino would have half-integer spin, a quantum mechanical property of matter, since the observed particles in β-decay did not conserve angular momentum. The existence of the neutrino and validation of Pauli's predictions would not experimentally verified for another 20 years.

The neutrino was first discovered in 1953 by Clyde Cowan and Frederick Reines using a nuclear reactor in South Carolina, U.S.A.. Since then three types of neutrinos have been observed and from unique sources like the Sun and a supernova. Neutrino physics continues to be an active region of physics since neutrinos are unique probes to processes otherwise inaccessible in laboratories. For instance in the depths of the Sun's core where fusion occurs and neutrinos are created, neutrinos are able to travel through the ultra dense and hot

[1]In W Pauli's December 1930 letter, he referred to his proposed particle as the "neutron", which is not the same neutron known of today. At that point in time, the neutral particles inside the atomic nucleus, also called "neutrons", had not been discovered, let alone understood. The neutron, which was discovered in 1932 by James Chadwick, has been formally associated as the neutral, cousin particle to the proton. It would be Enrico Fermi who would coin the particle in W Pauli's letter and solution to the β-decay spectrum as a "neutrino" meaning in Italian *little neutral one*.

medium of the core (over 10^7 degrees Kelvin) and outer layers of the Sun and reach us on Earth.

Neutrinos rarely interact with normal matter, meaning that they travel essentially unimpeded towards one's particle detector. The rarity of such interactions can be illustrated with the fact that given nearly 7.0×10^{10} neutrinos/cm^2/sec are incident on the Earth from the Sun[2], statistically one solar neutrino can harmlessly interact with an individual in her lifetime. So this begs the question: how does one detect a neutrino? The short answer is one needs a ultra large volume of matter and a large enough flux of neutrinos in its path just to detect one given today's technology.

Scientists continue to be interested in neutrinos due to properties they exhibit. One of the more recent and surprising aspects about neutrinos is their ability to undergo "flavor oscillations" where a neutrino of definite flavor (type) is created and later observed as a different flavor. The impact of such oscillations could help explain the observed matter and anti-matter asymmetry in the Universe.

1.1.1 Neutrinos in the Standard Model

The Standard Model (SM) of particle physics is the theory that describes the electromagnetic, strong nuclear, and weak nuclear forces and the elementary particles therein. These three forces and the gravitational force constitute the four *known* fundamental forces of the Universe. Each force in the SM has at least one "force carrier" particle that mediates the interactions between particles. The force carriers are formally called "gauge bosons" which indicates they are particles with integer $(0, 1, 2, ...)$ spin that come in temporary but unobservable existence to mediate the interaction. The weak nuclear bosons, the charged $W^{\pm}$ and neutral Z, couple to neutrinos as well as the other fermions, particles with half-integer

[2] To give some perspective to this number, this means 70 billion neutrinos are traveling every second through an area similar to one's own thumb nail.

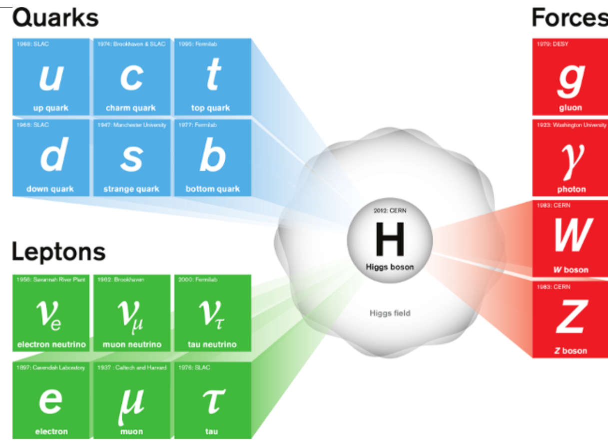

Figure 1.1: The Standard Model of particle physics consists of six quarks (up, down, strange, charm, bottom, and top), six leptons (electron, muon, tau, electron neutrino, muon neutrino, and tau neutrino), four force propagating bosons (gluon, photon, W, and Z), and the Higgs boson. The quarks, electron, muon, tau, W, and Z all gain mass through the Higgs field. The focus of this thesis are the neutrinos which are classified according to their charged, more massive Lepton cousins. Image taken from [6].

$\left(\frac{1}{2}, \frac{3}{2}, \frac{5}{2}, \ldots\right)$ spin, in the SM. All the elementary particles of the SM are shown in Figure 1.1 on page 4.

Neutrinos in the SM are electrically neutral, massless particles categorized into three generations based on their charged, more massive Lepton cousins. The neutrino and charged lepton pair into a "weak isospin doublet" in the SM. These doublets are locally gauge invariant under a SU(2)×U(1) symmetry which leads to the required existence of the photon and W and Z bosons[3].

What follows is a brief introduction to weak interactions. This is followed by a exploration on the nature of neutrino handedness. Then this is proceeded by a discussion on neutrino scattering with matter.

[3]A gauge theory describes ways to measure physical forces or fields through interactions between elementary particles. The electric or magnetic fields for example can only be probed by charged particles. In the realm of quantum field theories, fields are postulated to permeate everywhere and it is excitations of these fields which produce experimental observables. Fields are constructed using the Lagrangian formalism and altered using gauge transformations. If altering the Lagrangian in some way does not affect the observables, this is referred to as a gauge invariance. Local gauge invariance means that under the constraints of the experiment, certain gauge transformations do not affect the observables. The allowed locally gauge invariant transformations require knowledge of its underlying Lie, or symmetry, group. With the weak isospin doublets, the Lie groups are SU(2)×U(1) where SU(2) is the special unitary group of 2×2 unitary matrices, and U(1) is the unitary (circle) group consisting of complex numbers of magnitude 1.

1.1.1.1 Weak Interactions

The name "weak force" comes from the fact that this force is has a much smaller effective range than the electromagnetic, strong nuclear, and gravitational forces. This is due to the weak mediating bosons, the $W^{\pm}$ and Z, being massive particles unlike the massless gluon (g) and photon (γ). The W/Z have masses of 80/90 GeV/c^2, which is more massive than all the elementary particles except for the top quark.

For weak interactions to occur at energies far below the masses (also called "off-shell") of the W and Z, the interaction time must be infinitesimally small as dictated by the Heisenberg Uncertainty Principle

$$\Delta E \Delta t \gtrsim \hbar \tag{1.1}$$

where ΔE is the energy of the particle and Δt is the time which the particle exists. As an example, consider a neutrino of energy of 1 GeV emitting a Z-boson of off-shell energy, $\Delta E = 1$ GeV like shown in Figure 1.2 on page 6. The lifetime of that boson is about 10^{-25} seconds according to equation (**??**). In general, the probability that a massive particle of mass M will be created from the collision of two particles is given by a relativistic Breit–Wigner distribution

$$f(M) \propto \frac{1}{\left(\left(M^2 - M_0^2\right)c^4\right)^2 + \left(M_0 c^2 \Gamma\right)^2}, \tag{1.2}$$

where M_0 is the rest mass and Γ is the decay width of the particle in units of energy. For $M \ll M_0$, the probability of creating that particle will be infinitesimally small. Therefore to observe a single weak interaction requires a large amount of weakly interacting particles.

Weak interactions are classified into two classes of interactions: charged current (CC) and neutral current (NC). CC interactions involve a charged W boson and change the scattering neutrino into a electrically charged lepton of flavor l where the flavor of the neutrino ν_l is inferred from the charged lepton. The same cannot be said of NC interactions which exchange a neutral Z boson. NC interactions are flavor agnostic since they do not produce a charged lepton. An example of each interaction type is shown in Figure 1.2 on page 6.

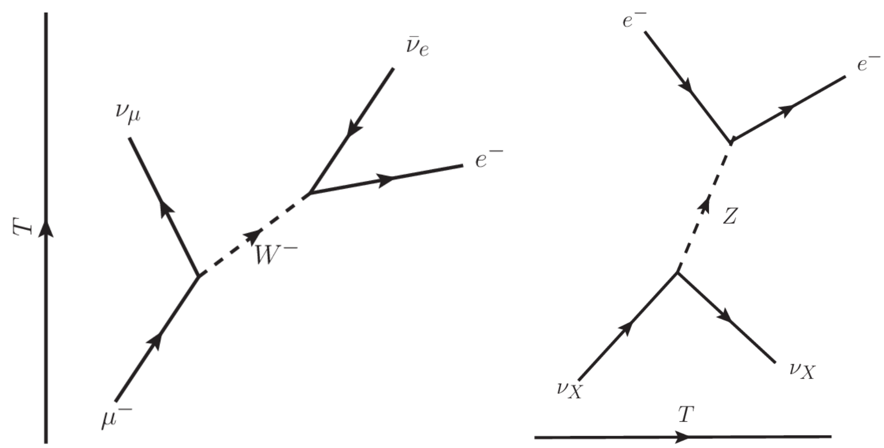

(a) Muon Decay **(b)** $\nu + e^-$ NC Scattering

Figure 1.2: (a) Muon decay $\left(\mu^- \to \nu_\mu \overline{\nu}_e e^-\right)$ Feynman diagram with time increasing from bottom to top. This is a charged current process that converts a muon into a muon neutrino via the emission of a W boson. Due to a conserved quantum number called lepton number, the W must emit an electron and electron neutrino pair. (b) Neutral current interaction Feynman diagram where time increases from left to right. This is a neutral current interaction where a neutrino of arbitrary flavor X scatters off an electron via the emission of a Z boson.

1.1.1.2 Chirality: How Neutrinos are Left Handed

Neutrinos are observed to have anti-parallel momentum vectors $\boldsymbol{P}$ to their spin vectors $\boldsymbol{\Sigma}$ and the opposite is true for anti-neutrinos. This property is called helicity and is given by (1.3)

$$\mathcal{H} = \frac{\boldsymbol{\Sigma} \cdot \boldsymbol{P}}{|\boldsymbol{P}|}. \tag{1.3}$$

While detecting neutrinos is hard as it is, the helicity is inferred from the daughter muon in charged pion decay. Since a pion has net zero (0) spin, the spin vectors of the daughters must also sum to zero. The muon from a π^+ decay has negative helicity (-1) hence the neutrino also has negative helicity. To confirm the anti-neutrino's helicity is positive (+1), the interaction requires both a charge (C) conjugation and parity (P) transformation as shown in Figure 1.3 on page 7. A C conjugation is a linear transformation that transforms all particles into their corresponding antiparticles while the P transformation inverts all spatial coordinates. Thus neutrinos are referred to *left-handed* (LH) particles while anti-neutrinos are *right-handed* (RH) particles. It turns out helicity is a useful quantum number to describe neutrinos and

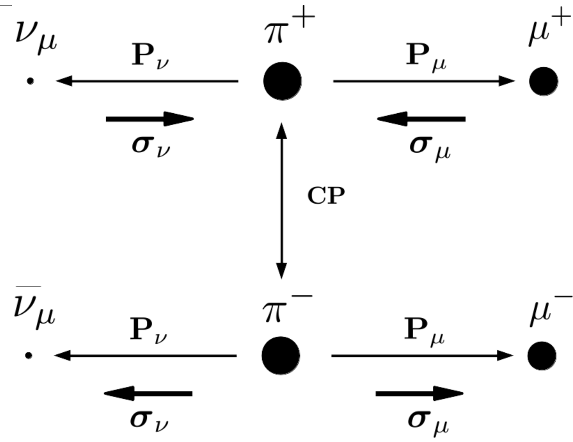

Figure 1.3: Decay of a charged pi meson into a muon and neutrino show the direction of the momentum $\boldsymbol{P}$ and spin $\boldsymbol{\sigma}$ of the outgoing particles. Since a pion at rest has zero (0) angular momentum, the system of daughter particles must have net zero angular momentum as well. A neutrino (antineutrino) is a right- (left-) handed helicity particle since its spin is (anti-)parallel to its momentum. Application of charge and parity (CP) converts all the particles into their respective antiparticles.

coincides with a property called chirality. To understand chirality and its relationship to helicity requires an analysis of the Dirac Lagrangian and Dirac equation.

The Dirac Lagrangian for a free particle field $\psi(x)$ with half-integer spin can be written as

$$\mathcal{L} = \overline{\psi}(x)\left[\frac{i\hbar}{2}\sum_{\mu=0}^{3}\gamma^\mu\left(\overrightarrow{\partial_\mu} - \overleftarrow{\partial_\mu}\right) - mc\right]\psi(x) \tag{1.4}$$

where $\psi(x)$ is a four-component vector (spinor) describing a particle field and γ^μ are a set of four 4×4 matrices. The adjoint field $\overline{\psi}(x)$ is defined as

$$\overline{\psi}(x) \equiv \psi^\dagger(x)\,\gamma^0 \tag{1.5}$$

where $\dagger$ denotes the conjugate and transpose operations. The $\overrightarrow{\partial_\mu}$ operator is a four-vector defined as

$$\partial_0 = \frac{1}{c}\frac{\partial}{\partial t}, \partial_1 = \frac{\partial}{\partial x}, \partial_2 = \frac{\partial}{\partial y}, \partial_3 = \frac{\partial}{\partial z} \tag{1.6}$$

that acts only on the right of it while $\overleftarrow{\partial_\mu}$ only acts on its left (i.e. $\overline{\psi}\overleftarrow{\partial_\mu} = \partial_\mu\overline{\psi}$). The γ^μ matrices are not unique and different representations dictate different kinematic regimes.

The field equations are extracted from the Lagrangian using the Euler-Lagrange procedure. In general for a set of M fields, the field equation are given by

$$\partial_\mu \frac{\partial \mathcal{L}}{\partial \left(\partial_\mu \psi_r\right)} - \frac{\partial \mathcal{L}}{\partial \psi_r} = 0 \quad (r = 0, 1, 2, \ldots, M-1, M)\,. \tag{1.7}$$

For the Dirac Lagrangian, the field equation for ψ is given by

$$\partial_\mu \frac{\partial \mathcal{L}}{\partial \left(\partial_\mu \overline{\psi}\right)} - \frac{\partial \mathcal{L}}{\partial \overline{\psi}} = 0 \tag{1.8}$$

which yields the Dirac equation

$$\left[i\hbar \sum_{\mu=0}^{3} \gamma^\mu \partial_\mu - mc \right] \psi\left(x\right) = 0. \tag{1.9}$$

The representation of the γ^μ matrices that is useful to describe neutrinos is the *Chiral representation* (also called the *Weyl representation*) where

$$\gamma^0 = \begin{bmatrix} 0 & I_2 \\ -I_2 & 0 \end{bmatrix}, \gamma^1 = \begin{bmatrix} 0 & \sigma_x \\ -\sigma_x & 0 \end{bmatrix}, \gamma^2 = \begin{bmatrix} 0 & \sigma_y \\ -\sigma_y & 0 \end{bmatrix}, \gamma^3 = \begin{bmatrix} 0 & \sigma_z \\ -\sigma_z & 0 \end{bmatrix}, \tag{1.10}$$

I_2 is the 2×2 identity matrix, $\sigma_{x,y,z}$ are the Pauli Spin matrices given by

$$\sigma_x = \sigma_1 = \begin{pmatrix} 0 & 1 \\ 1 & 0 \end{pmatrix}, \quad \sigma_y = \sigma_2 = \begin{pmatrix} 0 & -i \\ i & 0 \end{pmatrix}, \quad \sigma_z = \sigma_3 = \begin{pmatrix} 1 & 0 \\ 0 & -1 \end{pmatrix}.$$

Using the Chiral representation, the chirality matrix, γ^5 (the fifth gamma matrix), is defined as

$$\gamma^5 = i\gamma^0\gamma^1\gamma^2\gamma^3 = \begin{bmatrix} I_2 & 0 \\ 0 & -I_2 \end{bmatrix}, \tag{1.11}$$

which is diagonal as well as Hermitian meaning that its eigenvalues are real and observable. Let eigenfunctions of the chirality matrix be denoted with subscripts P and M such that the eigenvalue equations are

$$\begin{aligned}\gamma^5\psi_P &= +1\psi_P,\\ \gamma^5\psi_M &= -1\psi_M.\end{aligned} \tag{1.12}$$

The field equation solutions to (1.9) can be decomposed into ψ_P and ψ_M projections using two chiral projection operators $\hat{O}_{P,M}$ where

$$\psi = \left(\hat{O}_P + \hat{O}_M\right)\psi = \psi_P + \psi_M. \tag{1.13}$$

The chiral operators are explicitly given by

$$\begin{aligned}\hat{O}_M &= \frac{1}{2}\left(I_4 - \gamma^5\right) = \begin{pmatrix} 0 & 0 \\ 0 & I_2 \end{pmatrix},\\ \hat{O}_P &= \frac{1}{2}\left(I_4 + \gamma^5\right) = \begin{pmatrix} I_2 & 0 \\ 0 & 0 \end{pmatrix},\end{aligned} \tag{1.14}$$

where I_4 is the 4×4 identity matrix. Taken together (1.13) and (1.14) indicate the free neutrino field is a vector ψ minus axial vector $\gamma^5\psi$, also referred to as V-A, under P transformations. This feature is what allows for the weak force to violate P-symmetry and CP-symmetry. Referring back to(1.4) and (1.7), the Dirac equation becomes a set of coupled equations

$$\begin{aligned}i\hbar\sum_{\mu=0}^{3}\gamma^\mu\partial_\mu\psi_P &= mc\psi_M,\\ i\hbar\sum_{\mu=0}^{3}\gamma^\mu\partial_\mu\psi_M &= mc\psi_P\end{aligned} \tag{1.15}$$

where dynamics are set by the mass.

Since the chiral projection operators are decompositions of the identity matrix, the simplest nontrivial solution to ψ is

$$\psi = \begin{pmatrix} \chi_P \\ \chi_M \end{pmatrix} \tag{1.16}$$

where χ represent two-component spinors. Using 1.16 the Dirac equation in (1.15) can again be rewritten as

$$\begin{aligned} i\hbar\left[\frac{1}{c}\frac{\partial}{\partial t}+\boldsymbol{\sigma}\cdot\boldsymbol{\nabla}\right]\chi_P &= -mc\chi_M, \\ i\hbar\left[\frac{1}{c}\frac{\partial}{\partial t}-\boldsymbol{\sigma}\cdot\boldsymbol{\nabla}\right]\chi_M &= -mc\chi_P, \end{aligned} \tag{1.17}$$

where

$$\boldsymbol{\sigma}\cdot\boldsymbol{\nabla}=\sigma_x\frac{\partial}{\partial x}+\sigma_y\frac{\partial}{\partial y}+\sigma_z\frac{\partial}{\partial z}. \tag{1.18}$$

In the limiting case of vanishing mass ($m \to 0$), as is in the SM, the free particle field equations in (1.17) decouple into

$$\begin{aligned} \left(\frac{E}{c}+\boldsymbol{\sigma}\cdot\boldsymbol{P}\right)\chi_P &= 0, \\ \left(\frac{E}{c}-\boldsymbol{\sigma}\cdot\boldsymbol{P}\right)\chi_M &= 0, \end{aligned} \tag{1.19}$$

where the differential operators have been evaluated as the particle's energy E and momentum three-vector $\boldsymbol{P}$. For massless neutrinos, χ_P and hence ψ_P, describe particles of negative energy $E=-|\boldsymbol{P}|\,c$ which in the context of quantum field theory are interpreted as antiparticles traveling backwards in time. Conversely, ψ_M have positive energy $E=|\boldsymbol{P}|\,c$ and which means they are particles traveling forward in time.

If one also multiplies (1.15) by $\gamma^5\gamma^0$ and using the fact that the spin operator $\boldsymbol{\Sigma}$ is

$$\boldsymbol{\Sigma}=i\left(\gamma^2\gamma^3,\gamma^3\gamma^1,\gamma^1\gamma^2\right)=\gamma^0\gamma^k\gamma^5 \quad (k=1,2,3) \tag{1.20}$$

each decoupled equation becomes

$$\frac{\boldsymbol{\Sigma}\cdot\boldsymbol{P}}{|\boldsymbol{P}|}\psi_{P,M}=\gamma^5\psi_{P,M}=\pm\psi_{P,M}, \tag{1.21}$$

where one recognizes that helicity and chiral states are the same for $m \to 0$ only. Thus the labels M and P actually are identical to the LH and RH helicity labels, respectively. Using

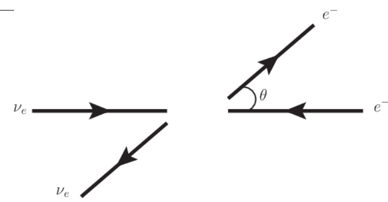

Figure 1.4: The definition of θ in $\nu_e + e^-$ (shown) and $\overline{\nu}_e + e^-$ (not shown) scattering.

the results on helicity from before, a neutrino is always observed as a LH particle while the anti-neutrino is always observed as a RH antiparticle.

The observation of only LH neutrinos and RH anti-neutrinos is an important feature in the SM. However, since neutrinos are known to have mass from oscillations, it is theoretically possible to observe a RH neutrino and LH anti-neutrino. That would require boosting to a highly relativistic reference frame with respect to the laboratory.

1.1.1.3 Neutrino Scattering with Matter

Charged current (CC) neutrino interactions on nuclear particles are the interactions used in this thesis. These interactions produce an outgoing charged lepton and a variety of hadronic states. While interactions with valence electrons is possible, they are far less common in large, subatomic particle detectors. However, the physics of neutrino-electron scattering is very similar to neutrino-nucleus scattering.

Consider neutrino-electron scattering, the cross section for $\nu_e + e^-$ is given by

$$\frac{d\sigma}{d\Omega} = \left(\frac{G\hbar c}{2\pi}\right)^2 s, \tag{1.22}$$

where G is the Fermi constant and s is the center of mass energy squared. Due to the V-A nature of the Weak force, neutrinos couple to LH particles and RH antiparticles. The outgoing particles are isotropically distributed in the center-of-mass frame since the initial and final spin state of the system is $J = 0$. Compare equation (**??**) with the cross section for $\overline{\nu}_e + e^-$

$$\frac{d\sigma}{d\Omega} = \left(\frac{G\hbar c}{4\pi}\right)^2 (1-\cos\theta)^2 s, \tag{1.23}$$

where θ is the observed scattering angle of the electron as shown in Figure 1.4 on page 11. Since the total spin of the $\overline{\nu}_e + e^-$ system is $J = 1$ with z-projection $J_z = 1$, the antineutrino is preferentially forward scattered. Integrating over all angles, the cross sections come out to

$$\sigma\left(\overline{\nu}_e + e^-\right) = \frac{1}{3}\sigma\left(\nu_e + e^-\right).$$

The factor $1/3$ arises from the fact that angular momentum conservation forbids the $J_z = -1$ and 0 states for $\overline{\nu}_e + e^-$ scattering. The same $1/3$ factor arises between $\nu_\mu + d \to \mu^- + u$ and $\overline{\nu}_\mu + u \to \mu^+ + d$ scattering.

In neutrino-nuclear scattering, the simple picture of free quarks must be replaced with the reality of the nuclear medium. Interactions with a single quark are still possible, but nuclear effects can alter the products of the interactions. The kinematics of the particles involved can be altered as well as the existence of a particle can be change depending on the point of interaction. Distinctions must be made in neutrino physics between point-like interactions ($\nu_e + e^-$) and post "final state interactions" (FSI) which are observable in an experiment.

Neutrino-nuclear scattering presented in this thesis come in three primary CC varieties: quasi-elastic (CCQE), deep inelastic scattering (CCDIS), and single pion production (CC1π). CCQE interactions refer to the process where an incoming neutrino (antineutrino) and neutron (proton) produce a charged lepton and proton (neutron). This process is thought of classically to have approximate mass conservation between the proton-neutron states ($\Delta m = 1.29$ MeV/c^2). CCQE interactions are the lowest energy CC interaction with a nucleon. While CCQE models work well for low-Z atoms like hydrogen, they do not extend well into many nucleon atoms. CCDIS is a high energy transfer process that shatters the nucleus apart which has the observation of many post-FSI hadrons. Modeling CCDIS can be challenging due to FSI and the uncertainty of the possible initial states of the nucleus.

Finally CC1π interactions refer to processes where a post-FSI charged pion is experimentally observed presumably from the decay of resonance state like the $\Delta(1232)$ baryon. These interactions are not well understood currently since they occur in the transition between CCQE and CCDIS interaction modes.

1.1.2 Neutrino Oscillations

Neutrino oscillations are the observation of a neutrino produced of definite flavor and later observed as a different flavor. This phenomenon was first observed as a deficit of neutrinos for a number of atmospheric and solar neutrino experiments. The deficit also seemed more pronounced for atmospheric neutrinos as the distance from their source increased. For neutrino oscillations to occur, at least one neutrino must be massive. This observation firmly established that the SM is wrong with its prediction of massless neutrinos.

The first indication of neutrino oscillations was from the Ray Davis Homesteak Mine experiment which began in the 1960s. Ray Davis was an expert Chemist and designed a radiochemical experiment to measure the flux of neutrinos from Sun. The purpose of this experiment was to test John Bahcall's prediction of the fusion rate in the Sun and neutrino flux from it as well. Davis' experiment would need to operate for many years to collect enough statistics due to expected low capture rate. Measurements continued into the 1980s and showed that the flux of neutrinos as measured at Homesteak was about 1/3 the expected rate and became known as the "Solar Neutrino Problem." The primary solutions were either the the solar model was incorrect or the neutrino capture cross section is incorrect somehow. The Sudbury Neutrino Observatory (SNO) was able to resolve this problem by making a model-independent measurement of the solar neutrino flux. SNO observed a ν_eCC-to-NC ratio of 0.301 ± 0.033, which confirmed that only about 30% of neutrinos arrive as ν_e flavors on Earth. Saying this another way, the majority of neutrinos arrive as the wrong flavor [32].

Another outstanding problem emerged with measurements of atmospheric neutrinos, in particular muon and electron types. Atmospheric neutrinos are produced when high energy cosmic rays strike atmospheric particles. These cosmic ray collisions generate mostly pions and kaons that decay into neutrinos. When trying to measure the ν_μ/ν_e ratio and comparing that with expected ratio, there was another significant deficit. This was particularly a problem as a function of the zenith angle for the Super-Kamiokande (SK) experiment. SK is a 50kt tank of pure water lined with thousands of photomultiplier tubes designed to observe solar and atmospheric neutrinos. It was the first experiment to perform a neutrino oscillation analysis that successfully explained the deficit.

While the phenomenon of neutrino oscillations has been understood for almost three decades, it was not predicted since oscillations require the neutrino has mass. The reasons why neutrino oscillations require massive neutrinos are explained in the next subsection.

1.1.2.1 Two Flavor Derivation

The phenomenon of neutrino oscillations can be described with elementary, non-relativistic Quantum Mechanics. Beginning with the Schrödinger Equation in (1.24)

$$-\frac{\hbar}{i}\frac{d}{dt}\left|\nu(\mathbf{r},t)\right\rangle = \hat{H}\left|\nu(\mathbf{r},t)\right\rangle, \tag{1.24}$$

where $\hat{H}$ is the Hamiltonian for the physical system, one considers a massive neutrino of mass m_j in its rest frame (free particle). The Hamiltonian is diagonal in this case, which acting on $\left|\nu_j\right\rangle$ results in the eigenvalue equation

$$\hat{H}\left|\nu_j(\mathbf{r},t)\right\rangle = E_j\left|\nu_j(\mathbf{r},t)\right\rangle, \tag{1.25}$$

where E_j is the energy of the neutrino $\left|\nu_j\right\rangle$. Substituting (1.25) into (1.24) and solving for $\left|\nu(\mathbf{r},t)\right\rangle$, one obtains the following

$$\left|\nu_j(\mathbf{r},t)\right\rangle = e^{-iE_jt/\hbar}\left|\nu_j(\mathbf{r},t=0)\right\rangle, \tag{1.26}$$

where $\left|\nu_j(\mathbf{r}, t=0)\right\rangle$ is created with momentum $\mathbf{p}$ at the origin $\mathbf{r}=0$. The time-independent solution to (1.24) is a plane-wave given by

$$\left|\nu_j(\mathbf{r}, t=0)\right\rangle = e^{i\mathbf{p}\ \cdot\ \mathbf{r}/\hbar}\left|\nu_j\right\rangle. \tag{1.27}$$

Before being able to describe neutrino oscillations, the basis states must be defined. For this example, consider that there are only two eigenstates, labeled ν_1 and ν_2, in the "mass" basis with definite mass m_1 and m_2, respectively. However, experiments can produce neutrinos, as well as probe them, only of definite "flavor", denoted by a Greek letter subscript λ. Let the generated neutrino, which is a linear superposition of mass states 1 and 2, have momentum $\mathbf{p}$ and flavor α. Since both mass eigenstates share the same momentum momentum $\mathbf{p}$ (but not energy!), the exponential term in (1.27) is an overall phase that will cancel out later. One can postulate a linear transformation, U, between the basis states given by (1.28).

$$\begin{bmatrix} \nu_\alpha \\ \nu_\beta \end{bmatrix} = \begin{bmatrix} U_{11} & U_{12} \\ U_{21} & U_{22} \end{bmatrix} \begin{bmatrix} \nu_1 \\ \nu_2 \end{bmatrix} \tag{1.28}$$

This linear transformation must be a unitary matrix $\left(U^{-1} = U^\dagger, \dagger = \text{transpose conjugate}\right)$ since the states $\nu_{1,2}$ constitute a complete orthonormal basis in the mass basis. With this unitary property, U can be written as a rotation matrix

$$\begin{bmatrix} \nu_\alpha \\ \nu_\beta \end{bmatrix} = \begin{bmatrix} \cos(\theta) & \sin(\theta) \\ -\sin(\theta) & \cos(\theta) \end{bmatrix} \begin{bmatrix} \nu_1 \\ \nu_2 \end{bmatrix}, \tag{1.29}$$

where θ is the angle between the two bases. One can imagine this transformation between bases as shown in Figure 1.5 on page 16 . Creating a neutrino of flavor α and observe it after a time $t = T > 0$, the probability of observing it as flavor $\beta \neq \alpha$ is given by

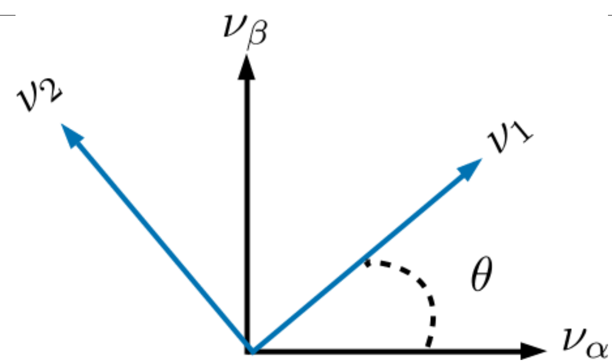

Figure 1.5: The depiction of two neutrino flavor change of basis using a rotation matrix. Compare this with equation (**??**).

$$\begin{aligned} \mathcal{P}\left(\nu_\alpha \to \nu_\beta\right) &= \left|\langle \nu_\alpha(t=0) | \nu_\beta(t=T)\rangle\right|^2 \\ &= |(\cos(\theta)\,\langle \nu_1(t=0)| + \sin(\theta)\,\langle \nu_2(t=0)|) \\ &\times\, (-\sin(\theta)\,|\nu_1(t=T)\rangle + \cos(\theta)\,|\nu_2(t=T)\rangle)|^2\,. \end{aligned} \tag{1.30}$$

Evaluating all inner products and simplifying terms in (1.30) results in (1.31) below.

$$\mathcal{P}\left(\nu_\alpha \to \nu_\beta\right) = \sin^2(2\theta)\sin^2\left(\frac{E_1 - E_2}{2\hbar}T\right) \tag{1.31}$$

The terminology of "neutrino oscillations" should be more apparent now since (1.31) demonstrates that the probability changes sinusoidally. This equation is not, however, terribly useful in the laboratory frame since it is hard to design an experiment where the travel time an individual neutrino is well known. Instead, one can make useful approximations that are accessible in the laboratory frame. Since neutrinos are nearly massless, they travel very close to the speed of light. Therefore time T is replaced with L/c where L is the distance between the neutrino origin and detection and c is now the speed of light in vacuum. One can also approximate the energy of the mass eigenstate as

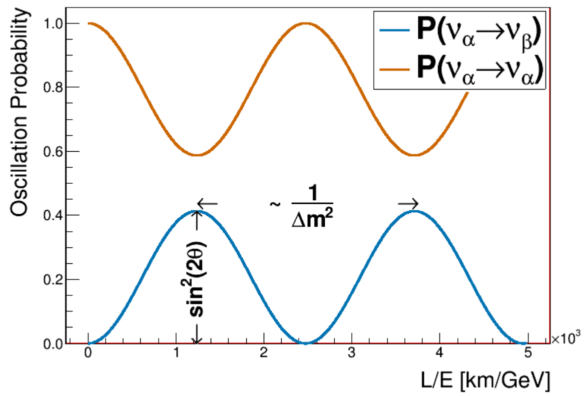

Figure 1.6: Two flavor oscillation probability as a function L/E is shown using $\theta = 20^{\circ}$ and $\Delta m^2 = 10^{-3}$ eV^2/c^4. The spacing between adjacent peaks/troughs is proportional to the inverse of Δm^2. Note that $\mathcal{P}\left(\nu_\alpha \to \nu_\alpha\right) = 1 - \mathcal{P}\left(\nu_\alpha \to \nu_\beta\right)$ since the oscillation probability must always sum to 1.

$$\begin{aligned} E_j = \left(m_j^2 c^4 + p_j^2 c^2\right)^{\frac{1}{2}} &= p_j c \left(1 + \frac{m_j^2 c^2}{p_j^2}\right)^{\frac{1}{2}} \\ &\approx p_j c \left(1 + \frac{m_j^2 c^2}{2 p_j^2} + \mathcal{O}\left(\frac{m_j c}{p_j}\right)^4\right) \\ &\approx E_\nu + \frac{m_j^2 c^4}{2 E_\nu}, \end{aligned} \tag{1.32}$$

where for oscillation experiments $p_j \gg m_j c$ and $p_j c \approx E_\nu$ where E_ν is the neutrino energy as measured in the laboratory. Substituting these assumptions in (1.31), the oscillation probability is given by

$$\mathcal{P}\left(\nu_\alpha \to \nu_\beta\right) = \sin^2(2\theta) \sin^2\left(\frac{\Delta m^2 c^3}{4\hbar} \frac{L}{E_\nu}\right), \tag{1.33}$$

where $\Delta m^2 = m_2^2 - m_1^2$ is the mass-squared difference between the mass states. For a momentum consider evaluating all the physical constants in natural units ($c = \hbar = 1$). An appropriate choice of units for Δm^2, L, and E_ν results in

$$\mathcal{P}\left(\nu_\alpha \to \nu_\beta\right) = \sin^2(2\theta) \sin^2\left(1.27 \frac{\Delta m^2}{\left[\mathrm{eV}^2\right]} \frac{{}^{L}\!/_{E_\nu}}{\left[{}^{\mathrm{km}}\!/_{\mathrm{GeV}}\right]}\right) \text{ [natural units]} \tag{1.34}$$

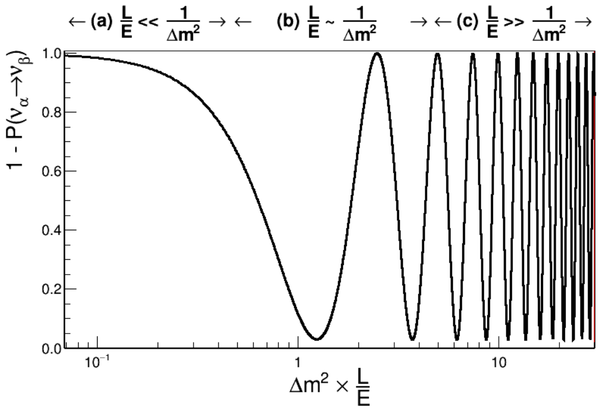

Figure 1.7: Logarithmic plot of the survival probability of flavor α $(1 - \mathcal{P}(\nu_\alpha \to \nu_\beta) = \mathcal{P}(\nu_\alpha \to \nu_\alpha))$ over a wide range of L/E values for $\theta = 40^\circ$. The arrows above the plot very roughly denote three possible cases: (a) no oscillations ($L/E \ll 1/\Delta m^2$); (b) sensitivity to oscillations ($L/E \sim 1/\Delta m^2$); (c) only average measurement ($L/E \gg 1/\Delta m^2$). Image originally inspired by [27].

which more clearly demonstrates the Physics in neutrino oscillations. The oscillation probability has an amplitude of $\sin^2(2\theta)$ and varies with frequency inversely proportional to Δm^2 as illustrated in Figure 1.6 on page 17. Since L and E_ν are the only controllable parameters for an oscillation experiment, probing θ or Δm^2 can be difficult unless the experiment can probe a large range of L/E_ν as shown in Figure 1.7 on page 18.

1.1.2.2 Three Flavor Oscillations

In the general case of oscillations using a $n \times n$ mixing matrix, the unitary transformation can be written as a rotation matrix with $\frac{n}{2}(n-1)$ weak mixing angles with $\frac{1}{2}(n-2)(n-1)$ Charge-Parity (CP) violating phases. In addition, oscillations are dictated by a total of $n-1$ mass-squared splittings [32]. This all assumes that neutrinos obey the Dirac Equation, or that they are not their own antiparticles. The favored mixing model is the 3×3 matrix since there are three known neutrino flavors, ν_e, ν_μ, and ν_τ. This means that there are three (3) mixing angles, one (1) CP violating phase, and three (3) mass-squared splittings.

The most frequently used matrix parameterization is the MNSP (MNSP: Maki-Nakagawa-Sakata-Pontecorvo) matrix. Pontecorvo is accredited for first conceiving of neutrino oscilla-

Source	Species	Baseline [km]	Mean Energy [GeV]	$\min\left(\Delta m^2\right)\ \left[\mathrm{eV}^2\right]$
Reactor	$\overline{\nu}_e$	1	$\sim 10^{-3}$	$\sim 10^{-3}$
Reactor	$\overline{\nu}_e$	100	$\sim 10^{-3}$	$\sim 10^{-5}$
Accelerator	$\nu_\mu, \overline{\nu}_\mu$	1	~ 1	~ 1
Accelerator	$\nu_\mu, \overline{\nu}_\mu$	10^3	~ 1	$\sim 10^{-3}$
Atmospheric ν's	$\nu_{e,\mu}, \overline{\nu}_{\mu,e}$	10^4	~ 1	$\sim 10^{-4}$
Sun	ν_e	1.5×10^8	$\sim 10^{-3}$	$\sim 10^{-11}$

Table 1.1: Sensitivity of different oscillation experiments originally published in [29].

tions, albeit between neutrino and anti-neutrinos [24]. It was Maki, Nakagawa, and Sakata who conceived of the parameterization based off the ideas of Pontecorvo [23]. The MNSP matrix is decomposed into separate rotation matrices as given by (1.35)

$$U_{\mathrm{MNSP}} = \overbrace{\begin{bmatrix} 1 & 0 & 0 \\ 0 & c_{32} & s_{32} \\ 0 & -s_{32} & c_{32} \end{bmatrix}}^{U_{\mathrm{atm}}} \times \overbrace{\begin{bmatrix} c_{31} & 0 & s_{31}e^{i\delta_{\mathrm{CP}}} \\ 0 & 1 & 0 \\ -s_{31}e^{-i\delta_{\mathrm{CP}}} & 0 & c_{31} \end{bmatrix}}^{U_{\mathrm{rea}}} \times \overbrace{\begin{bmatrix} c_{21} & s_{21} & 0 \\ -s_{21} & c_{21} & 0 \\ 0 & 0 & 1 \end{bmatrix}}^{U_{\mathrm{sol}}}, \tag{1.35}$$

where

$$c_{ij} = \cos\theta_{ij}, \quad s_{ij} = \sin\theta_{ij}, \tag{1.36}$$

and δ_{CP} represents the CP violating phase. Each rotation matrix represents the different sources for neutrino oscillations experiments with “atm”, “rea”, and “sol” representing atmospheric ν's, nuclear reactor ν's, and Solar ν's, respectively. The sensitivity of neutrino oscillations for different sources is given in Table 1.1 on page 19.

If neutrinos are their own antiparticles, they do not follow the Dirac Equation but do follow the Majorana Equation. This adds two (in general $n-1$) more CP violating Majorana phases, α and β, to the MNSP matrix

$$U_{\mathrm{MNSP}} \rightarrow U_{\mathrm{MNSP}} \times \overbrace{\begin{bmatrix} 1 & 0 & 0 \\ 0 & e^{i\alpha} & 0 \\ 0 & 0 & e^{i\beta} \end{bmatrix}}^{U_{\mathrm{Majorana}}} . \tag{1.37}$$

Unfortunately, neutrino oscillations are not able to probe the Majorana phases since the Majorana matrix is diagonal. The question of if neutrinos are Majorana ($\nu = \overline{\nu}$) or Dirac ($\nu \neq \overline{\nu}$) particles is an open question and is being explored by non-oscillation experiments.

The full three flavor oscillation probability is given by

$$\begin{aligned} \mathcal{P}\left(\nu_\alpha \rightarrow \nu_\beta\right) = \delta_{\alpha\beta} - 4\sum_{j=1}^{3}\left[\sum_{i>j}^{3} \mathrm{Re}\left(K_{\alpha\beta,ij}\right)\sin^2\left(\phi_{ij}\right)\right] \\ +4\sum_{j=1}^{3}\left[\sum_{i>j}^{3} \mathrm{Im}\left(K_{\alpha\beta,ij}\right)\sin\left(\phi_{ij}\right)\cos\left(\phi_{ij}\right)\right] \end{aligned} \tag{1.38}$$

where

$$K_{\alpha\beta,ij} = U_{\alpha i}U^{*}_{\beta_i}U^{*}_{\alpha j}U_{\beta j} \tag{1.39}$$

encapsulates the MNSP matrix elements and

$$\phi_{ij} = \frac{\Delta m^2_{ij}c^3}{4\hbar}\frac{L}{E_\nu}. \tag{1.40}$$

Since CP violation means that $\mathcal{P}\left(\nu_\alpha \rightarrow \nu_{\beta\neq\alpha}\right) \neq \mathcal{P}\left(\overline{\nu}_\alpha \rightarrow \overline{\nu}_{\beta\neq\alpha}\right)$, CP violating terms must be an odd function of δ_{CP}. Consider the following examples, muon neutrino survival and muon neutrino to electron neutrino appearance.

1.1.2.2.1 Muon Neutrino Survival The probability of a muon type neutrinos surviving is given by

$$\begin{aligned} \mathcal{P}\left(\overset{(-)}{\nu}_\mu \rightarrow \overset{(-)}{\nu}_\mu\right) = 1 - 4s^2_{23}c^2_{13}\left(V_{\cos\delta_{\mathrm{CP}}}\right)\sin^2\phi_{31} \\ -4s^2_{23}c^2_{13}\left(Z_{\cos\delta_{\mathrm{CP}}}\right)\sin^2\phi_{32} \\ -4\left(V_{\cos\delta_{\mathrm{CP}}}\right)\left(Z_{\cos\delta_{\mathrm{CP}}}\right)\sin^2\phi_{21} \end{aligned} \tag{1.41}$$

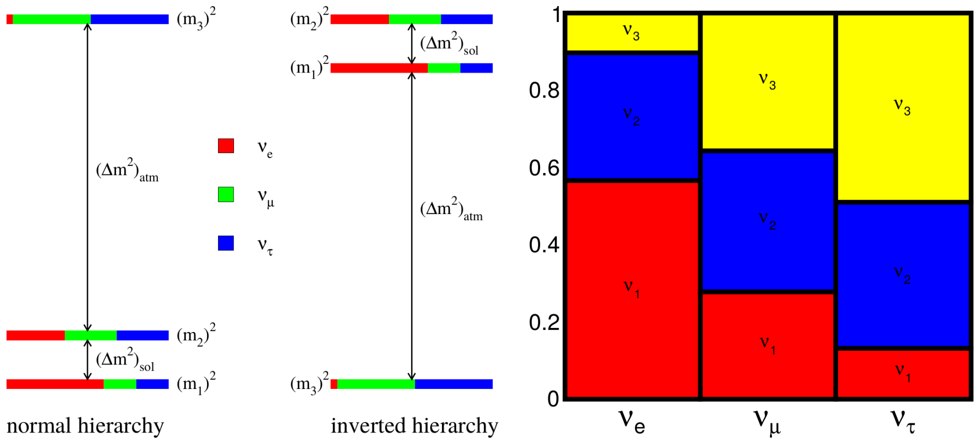

(a) Mass hierarchy as shown in [13]

(b) Mass eigenstate components as shown in [6]

Figure 1.8: Left: the mass hierarchy problem is such that while the solar and atmospheric mixing mass-squared differences are clearly defined, the absolute mass scale is unknown. Since $m_2 > m_1$ by definition, it is currently unknown if m_3 is more or less massive than m_2, or even massless! Notice the colored bars for each mass eigenstate which corresponded to the approximate flavor content of the neutrino. For example, state "2" has about equal three portions of all three flavors. Right: the mass eigenstate components of each flavor eigenstate. This is a complementary demonstration of the MNSP matrix.

where

$$V_{\cos\delta_{\rm CP}} = s_{12}^2 c_{23}^2 + s_{13}^2 s_{23}^2 c_{12}^2 + 2 s_{12} s_{13} s_{23} c_{12} c_{23} \cos\delta_{\rm CP} \tag{1.42}$$

$$Z_{\cos\delta_{\rm CP}} = c_{12}^2 c_{23}^2 + s_{13}^2 s_{23}^2 s_{12}^2 - 2 s_{12} s_{13} s_{23} c_{12} c_{23} \cos\delta_{\rm CP} \tag{1.43}$$

and $\overset{(-)}{\nu}_\mu$ represents either ν_μ or $\overline{\nu}_\mu$. Since all CP violating terms in (1.41) are even functions of $\delta_{\rm CP}$, this channel does not offer insights into CP violation in a vacuum[4].

1.1.2.2.2 Electron Neutrino Appearance While CP violation is not observable in muon neutrino disappearance, it is with electron neutrino appearance. The appearance probability of electron neutrinos types from muon types is given by

[4]When going to through matter however, the oscillation probability is affected. This is explained more in Section 1.1.2.3.

$$\begin{aligned}\mathcal{P}\left(\overset{(-)}{\nu}_\mu \rightarrow \overset{(-)}{\nu}_e\right) =& 4c_{13}^2 s_{13}^2 s_{23}^2 \sin^2\phi_{31} \\ &+ 8\left(X_{\cos\delta_{\mathrm{CP}}}\right)\cos\phi_{23}\sin\phi_{31}\sin\phi_{21} \\ &\overset{(+)}{-} 8\underbrace{\left(Y_{\sin\delta_{\mathrm{CP}}}\right)}_{\text{CP violating}}\sin\phi_{32}\sin\phi_{31}\sin\phi_{21} \\ &+ 4\left(Z_{\cos\delta_{\mathrm{CP}}}\right)s_{12}^2 c_{13}^2 \sin^2\phi_{21}\end{aligned} \tag{1.44}$$

where

$$X_{\cos\delta_{\mathrm{CP}}} = c_{13}^2 s_{12} s_{13} s_{23}\left(c_{12}c_{23}\cos\delta_{\mathrm{CP}} - s_{12}s_{13}\right) \tag{1.45}$$

$$Y_{\sin\delta_{\mathrm{CP}}} = \frac{1}{8}\sin\left(2\theta_{12}\right)\sin\left(2\theta_{13}\right)\sin\left(2\theta_{23}\right)c_{13}\sin\delta_{\mathrm{CP}} \tag{1.46}$$

and (+) represents the sign change from neutrinos to anti-neutrinos. The CP violating term (1.46) is also known as the Jarlskog Invariant and is a measure of CP violation independent of the mixing parameterization [20]. This oscillation channel are of primary importance in accelerator and atmospheric neutrino oscillation experiments.

Current and next generation experiments aim to improve knowledge of the mixing parameters. There are a couple of degeneracies to unravel as well as precise measurement of δ_{CP}. While the two defined mass-squared splittings $\Delta m_{21}^2 = \Delta m_{\mathrm{sol}}^2$ and $\Delta m_{32}^2 = \Delta m_{\mathrm{atm}}^2$ are known, it is unknown which eigenstates are more massive. This problem is known as the mass hierarchy problem and is illustrated in Figure 1.8a on page 21. Normal hierarchy refers to the case where $m_3 > m_2 > m_1$whereas the inverted hierarchy has $m_2 > m_1 > m_3$. Also knowledge if θ_{23} is in the first octant $\theta \in (0, \pi/2)$ or second octant $\theta \in (\pi/2, \pi/4)$ requires large statistics. Finally the value of δ_{CP} is quite uncertain with values in the 3rd and 4th quadrants. Best fit measurements of the oscillations parameters is given in Table 1.2 on page 23.

Parameter	Normal Hierarchy value	Inverted Hierarchy value	Units
$\Delta m^2_{32} = \Delta m^2_{\text{atm}}$	2.51 ± 0.05	-2.56 ± 0.04	10^{-3} eV^2
$\Delta m^2_{21} = \Delta m^2_{\text{sol}}$	7.53 ± 0.18		10^{-5} eV^2
$\sin^2(\theta_{21})$=$\sin^2(\theta_{\text{sol}})$	$0.307^{+0.013}_{-0.012}$		1
$\sin^2(\theta_{32})$=$\sin^2(\theta_{\text{atm}})$	O1: $0.417^{+0.025}_{-0.028}$ O2: $0.597^{+0.024}_{-0.030}$	O1: $0.421^{+0.033}_{-0.025}$ O2: $0.592^{+0.023}_{-0.030}$	1
$\sin^2(\theta_{31})$	2.12 ± 0.08		10^{-2}
δ_{CP}	217^{+40}_{-28}	280^{+25}_{-28}	degrees

Table 1.2: Table of best fit MNSP parameters split by normal and inverted hierarchy. O1 and O2 correspond to the first octant ($\theta \in (0, \pi/2)$) or second octant ($\theta \in (\pi/2, \pi/4)$). All values except for δ_{CP} are combined values from the Particle Data Group and δ_{CP} is from the 2018 NuFit analysis [14,29].

1.1.2.3 Matter Effects

Traveling through matter has the potential to increase the sensitivity of oscillation measurements if the baseline is long enough. Known as the Mikheyev-Smirnov-Wolfenstein (MSW) effect, all oscillations are affected by coherent forward scattering of neutrinos with electrons in the media. Taking the example of $\overset{(-)}{\nu}_\mu \rightarrow \overset{(-)}{\nu}_e$ from (1.41), the MSW effect to first order is

$$\begin{aligned}\mathcal{P}\left(\overset{(-)}{\nu}_\mu \rightarrow \overset{(-)}{\nu}_e\right) \rightarrow & \mathcal{P}\left(\overset{(-)}{\nu}_\mu \rightarrow \overset{(-)}{\nu}_e\right) + \frac{8\alpha}{\Delta m^2_{31}}\left(c^2_{13}s^2_{13}s^2_{23}\right)\left(1-2s^2_{13}\right) \\ & \times \left(\sin^2\phi_{31} \overset{(+)}{-} \underbrace{\left(\frac{\Delta m^2_{31}c^3}{4\hbar}\frac{L}{E_\nu}\right)}_{\phi_{31}} \cos\phi_{32}\sin\phi_{31}\right),\end{aligned} \tag{1.47}$$

where

$$\alpha = 2\sqrt{2}G_F n_e E_\nu \tag{1.48}$$

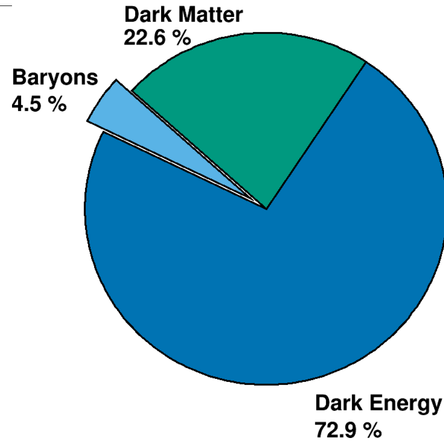

Figure 1.9: Matter and energy content of the Universe display that while the Universe consists of 4.5% of baryonic matter. The rest of the Universe consists of non-baryonic matter called Dark Matter and a form of energy called Dark Energy. These inferred parameters are taken from the ΛCDM model, the simplest model that describes the cosmos [21].

and G_F is the Fermi constant and n_e is the average electron density of the Earth which the neutrinos travel [7]. Carefully studying (1.47) reveals that the MSW effect alters the oscillation probability as a function of the electron density and increases in magnitude with baseline.

1.1.3 CP Violation: Origins of Matter

To conclude the introduction on neutrinos, it is important to examine the implications of CP violation. The observation of CP violation in the lepton sector might provide critical insight into the origins of the matter. CP violation dictates that certain interactions behave differently between matter or antimatter like $\mathcal{P}\left(\nu_\mu \rightarrow \nu_e\right) \neq \mathcal{P}\left(\overline{\nu}_\mu \rightarrow \overline{\nu}_e\right)$. The Big Bang Theory suggests that in the first fractions of a second of the Universe, equal amounts of matter and antimatter were created. However, observational evidence shows the Universe consists of only 4.5% baryonic matter (i.e. protons and neutrons) from cosmological models as shown in Figure 1.9 on page 24. The anti-baryonic fraction of the baryonic matter is infinitesimally low from external constraints on data from gamma-ray telescopes like Fermi-GLAST [30]. This problem is known as the Baryon Asymmetry of the Universe (BAU).

The process of Baryogenesis[5] is a favored model to explain the BAU and lacks a necessary precursor mechanism. One of the necessary conditions for Baryogenesis [26] is C symmetry violation and CP violation. Evidence of CP violation has been experimentally confirmed in the quarks, but not to the level which resolves the BAU. Baryogenesis can be achieved by having Leptogenesis[6] occur first through the decay of very heavy, right handed Majorana neutrino ($\nu = \overline{\nu}$) through the *see-saw* mechanism. Detailed discussions on Leptogenesis and the *see-saw* mechanism can found in [6].

1.2 Tokai-to-Kamioka Experiment

The Tokai-to-Kamioka (T2K) experiment is a long baseline, neutrino oscillation experiment hosted in Japan [1] as shown in Figure 1.10 on page 26. It is the successor experiment to the KEK-to-Kamioka neutrino oscillation experiment also hosted in Japan. T2K produces its high intensity, muon neutrino pure beam at the Japan Proton Accelerator Complex (J-PARC), a world class particle accelerator facility. The beam is directed at the Super-Kamiokande (SK) [16] detector which is 295 km away from the source. Along the beamline at 280m from the beam source are a series of near detectors called ND280 [15] to observe and characterize the unoscillated beam. The beam is designed to maximize the $\nu_\mu \to \nu_e$ probability at the L =295 km baseline using a neutrino energy spectrum sharply peaked at $E_\nu = 0.6$ GeV as shown in Figure 1.11 on page 26. This spectrum is achieved by directing the center of the beam axis 2.5 degrees off center from SK.

T2K was primarily designed to measure the last unknown MNSP mixing angle θ_{13}, which was thought to be nearly zero. In addition it set out to measure to high precision the atmospheric mixing parameters, θ_{23} and Δm^2_{23}. One of its early successes was a landmark

[5] Baryogenesis is the mechanism by which matter and antimatter baryons are created in the early Universe.

[6] Leptogenesis is the mechanism by which leptons and anti-leptons are created in the early Universe.

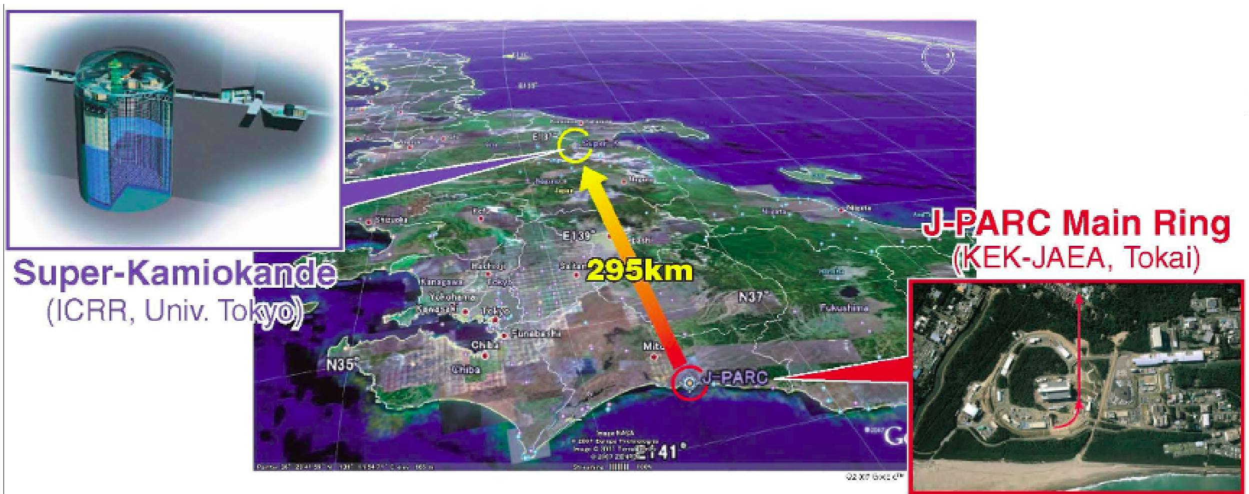

Figure 1.10: Birds eye view of the T2K experiment on the Japanese archipelago. An intense beam of neutrinos are produced at the J-PARC site (bottom right red box) using high energy protons. The beam is directed towards the Super-Kamiokande detector (top left blue box) at a distance of 295 km away from J-PARC.

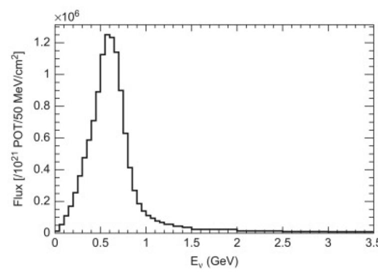

Figure 1.11: The T2K unoscillated ν_μ flux at SK at the off-axis angle of 2.5°.

7.3σ measurement of a non-zero θ_{13} using the electron-neutrino appearance measurement [3]. It continues to be a world leader in oscillation physics and as of 2018 rejects CP conserving values ($\delta_{\mathrm{CP}} = 0, \pi$) at the 2σ level [4].

The following topics will be discussed in the following order. First a look how neutrinos are produced at J-PARC. Next a detailed look at the T2K near detectors which are used in this thesis. This is followed by a discussion on Super-Kamiokande, the T2K far detector. The final topic is the basics of an oscillation analysis using a near and far detector.

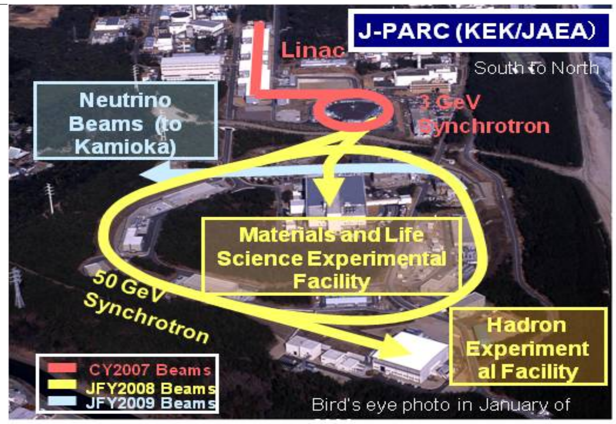

Figure 1.12: Bird's eye view of the J-PARC center showing the primary components of its accelerator programs. To generate the high intensity neutrino beam, first the linear accelerator (Linac, red) accelerates hydrogen ions (protons) into the 3 GeV Synchrotron (also red) called the rapid-cycle synchrotron (RCS). The RCS then injects some of its protons into the 50 GeV Synchrotron (yellow) called the main ring (MR) which currently runs at 30 GeV. Finally the MR protons are directed into a target material along the neutrino beamline (teal) [11].

1.2.1 Neutrino Production at J-PARC

To facilitate the high intensity neutrino beam requirements for T2K, the J-PARC site generates a high intensity proton beam through a series of particle accelerators. A bird's eye view of J-PARC can be seen in Figure 1.12 on page 27 which highlights its different accelerators and facilities. For this section, note that all beam energies are kinetic energies.

Protons for the T2K beamline are first accelerated in the J-PARC linear accelerator[7] (linac) and then the rapid cycle synchrotron[8] (RCS). Hydrogen ions ($^1_1\mathrm{H}^-$) are extracted from plasma in a electrical discharge chamber and feed through a series of linac elements as shown in Figure 1.13a on page 28. Each linac element except for the initial quadrapole magnet apparatus accelerates the ions using carefully coordinated oscillating electric fields generated by radio frequency pulses. After traveling 240m along the linac, the ions have been

[7] A linear accelerator accelerates particles using time varying electric fields along a one direction, terminal beamline. Not only used in particle physics, they are also used in the medical field to generate X-rays.

[8] A synchrotron is cyclic particle accelerator that relies on time varying magnetic fields to accelerate particles. Since they require many magnets and large spaces to operate, they are usually operated at national laboratories for others uses as well like material and life sciences.

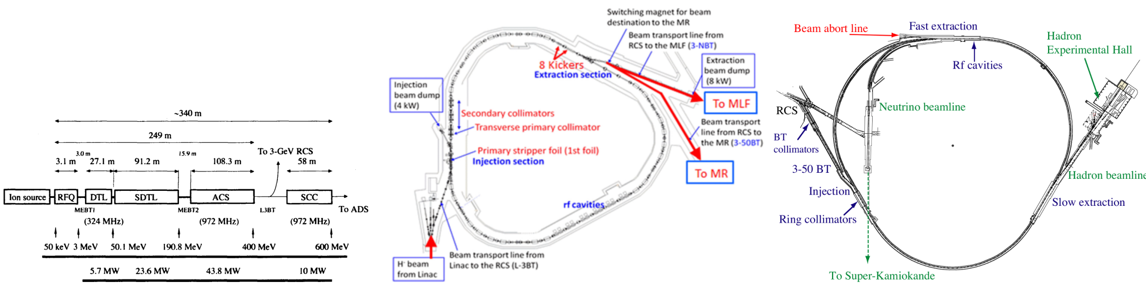

(a) 400 MeV linac

(b) 3 GeV RCS

(c) 50 GeV MR

Figure 1.13: Schematics of the J-PARC accelerators. (a) The linac accelerates hydrogen ions to 181 MeV of kinetic energy, designed for 400 MeV, from the ion source through linear accelerator (linac) elements [31]. (b) Protons from the linac are collected into the rapid cycle synchrotron (RCS) and accelerated to 3 GeV [25]. (c) Protons from the RCS are injected into the main ring (MR) synchrotron which further accelerates the protons. While the MR is designed for 50 GeV, it currently operates at 30 GeV. For T2K, the protons are bunched in the MR and extracted into the "Neutrino beamline" [19].

boosted to 181 MeV of kinetic energy and transported into the RCS. In transit to the RCS, the ions are stripped of their electrons via charge stripping foils. The 348m circumference RCS then further boosts the protons to 3 GeV at an operating frequency of 25 Hz. While being accelerated, protons are aggregated into two bunches and focused using particle collimators as shown in Figure 1.13b on page 28.

The next stage for the protons intended for the neutrino beamline is the much larger main ring (MR) synchrotron as shown in Figure 1.13c on page 28 which has a circumference of 1567m. While nominally designed to boost protons to 50 GeV, it currently operates at 30 GeV. Protons are injected into the MR to form eight proton bunches (spill), initially six when T2K first ran, before entering the neutrino beamline. The total temporal width of the spill is approximately 0.5μs [1]. At a spill cycle frequency of 0.5Hz, the bunches are extracted from the MR into the neutrino beamline.

The neutrino beamline is designed to direct the protons toward SK and generate neutrinos by impinging them on a cylindrical target. Figure 1.14a on page 29 shows the process of proton extraction from the MR for both primary and secondary neutrino beamlines. In the primary beamline, a series of normal and superconducting magnets steer the proton beam

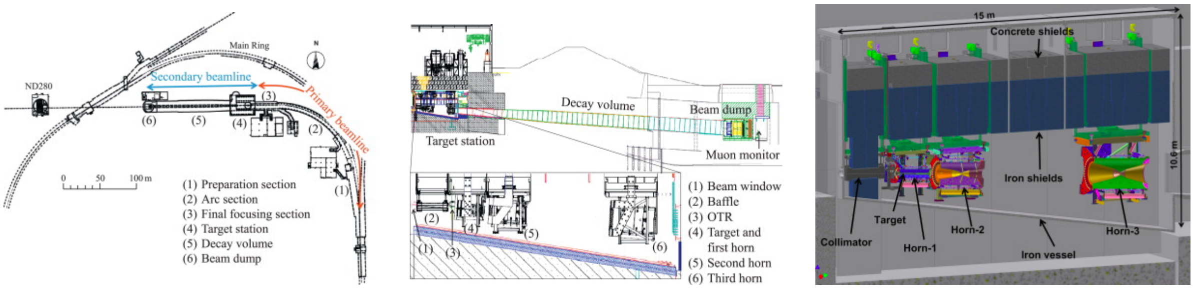

(a) Neutrino beamline **(b)** Secondary beamline **(c)** Beamline horns

Figure 1.14: The neutrino beamline at J-PARC consists of a primary and secondary beamline. (a) The primary beamline redirects the protons towards the secondary beamline [1]. (b) In the secondary beamline, the protons are impinged on a cylindrical target producing mostly pions. The pions are focused using in sequence horns and decay in a long decay volume. Any non-decayed particles are stopped at the beam dump. (c) A further zoomed in cross section of the target station showing the target and focusing horns [28].

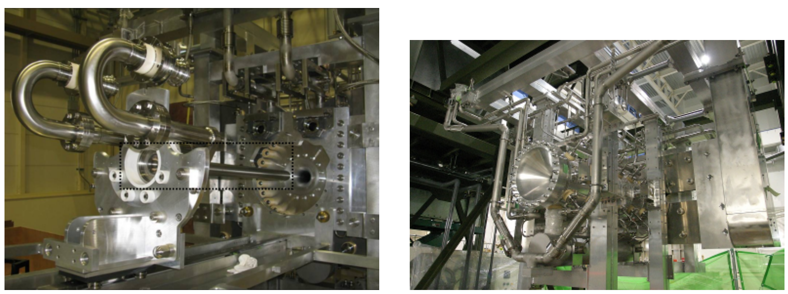

(a) A graphite target being extracted from the target station **(b)** A magnetic focusing horn

Figure 1.15: Shown are photos of work performed on the target station. (a) The graphite rod being extracted from the target station is shown in the black-dashed box. (b) One focusing horn in T2K.

away from the MR first along a 54m preparation section and then a 147m arc section to bend the beam towards SK. A final focusing section in the primary beamline focuses the protons into the secondary beam while directing it downwards 3.637° with respect to the local horizontal. Since a well tuned and stable proton beam is necessary for neutrino production, numerous beam monitors are installed along the primary beamline to measure any losses.

The secondary beamline marks the end of the proton beam and production of a neutrino beam. In the secondary beamline, as shown in Figure 1.14b on page 29, it consists of a target station, a decay volume for the outgoing particles from the target station, and a beam dump for any remaining particles. The target station houses a 91.4cm long, 2.6cm diameter, and

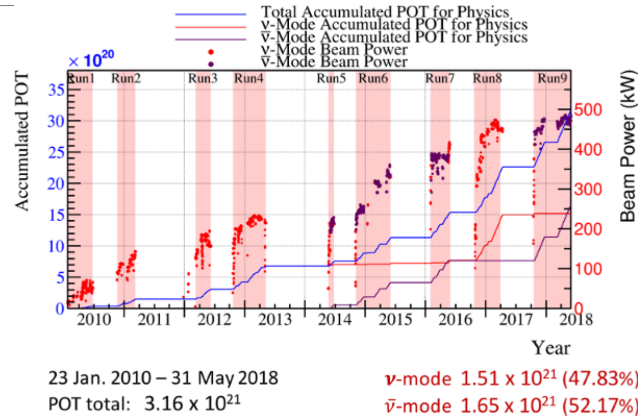

Figure 1.16: T2K accumulated protons on target since 2010 shows a steady increase in beam power over time. The gap between Run2 and Run3 is due to the damage suffered at J-PARC after the 2011 Tōhoku earthquake.

1.8g/cm^3 graphite rod which corresponds to 1.9 radiation lengths. When the protons impinge the target, strong (nuclear) interactions produce pi-mesons (pions) and ka-mesons (kaons). like those produced from cosmic ray collisions in the upper atmosphere. To enhance the flux of neutrinos, a series of three current pulsed, focusing magnets called horns[9] as shown in Figure 1.14c on page 29 are used to focus the mesons of the correct charge towards SK. Photographs of a graphite target and focusing horn are shown in Figure 1.15 on page 29. The horns are pulsed at +250kA (-250kA) to select positively (negatively) charged pions. The focused pions are allowed to decay along the 96m long decay volume as to boost the daughter neutrinos along the secondary beamline direction. For safety reasons, the decay volume is filled with gaseous helium at 1 atm of pressure which has a low pion absorption rate. The daughter particles in the decay volume should be mostly muons and muon-neutrinos traveling towards SK. An beam dump is placed at the end of the decay volume to stop particles that have not yet decayed to prevent uncontrolled for decay products from contaminating the beam.

Along both beamlines are numerous monitors and timing systems to observe the proton beam to ensure stable production of neutrinos. Proton beam monitors are placed along the

[9]The name horn derives from the fact that the focusing magnets are shaped like brass horns in a music ensemble or marching band. One can think of these horns like a focusing lens for charged particles.

primary beamline to ensure the proton beam is properly steered into the secondary beamline. An optical transition radiation monitor is situated around the target to observe any protons not intersecting with the target region itself. The last monitor along the secondary beamline is the a muon monitor (MUMON), which is placed downstream of the beam dump to observe the daughter muons of > 5 GeV/c momentum [1].

In order to provide timing information for the neutrino beam at SK, a global positioning system (GPS) is used to synchronize clocks at SK and J-PARC. Any event outside the beam timing window are rejected in the T2K oscillation analysis, and so having precise timing information for the neutrino beam is critical for the experiment. The GPS has an internal accuracy of 50ns, or about $\sim$ 150m assuming the neutrinos are traveling near the speed of light. This is well within the time it takes for any neutrino to travel the 295 km between J-PARC and SK.

J-PARC continues to improve the proton delivery and neutrino modes since T2K begin in 2010. T2K has run in two horn current modes: ν-mode and $\overline{\nu}_\mu$-mode. Focusing positively charged pions with +250 kA horn current is called forward horn current (FHC) mode. Similarly, using -250 kA horn current is called reverse horn current (RHC) mode. The aggregate running of T2K for both FHC and RHC modes are shown in Figure 1.16 on page 30 in units of protons on target (POT).

In addition the proton beam intensity, as measured in kW (energy/proton/second), has been increased over time which increases the number of neutrino interactions observed at SK. Note that while ± 250 kA is the preferred horn current in both FHC and RHC modes, the horns were run briefly at +205kA when operations resumed after 2011 Tōhoku earthquake.

1.2.2 Neutrino Near Detectors: ND280

T2K has a near detector (ND) site at J-PARC that is designed specifically observe the neutrinos in flight. The purpose of a ND site is due to large uncertainties from the neutrino flux in previous neutrino oscillation experiments. The site is called ND280 and is located

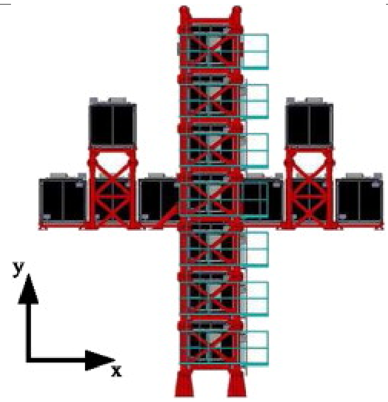

Figure 1.17: A schematic of INGRID shows the arrangement of the tracking scintillating modules. There are 16 identical modules total with seven in the vertical row, seven in the horizontal row, and two at off-axis positions. INGRID is capable of measuring the neutrino beam in a transverse area of 10m × 10 m. With the vertical row upstream of the horizontal row, the designed beam center intersects each row's center module [2].

280m away from the production target. The primary detector is an off-axis, magnetized tracking detector consisting of different subdetectors. A separate detector array called the Interactive Neutrino Grid (INGRID) measures the neutrino beam profile. Both on-axis and off-axis detectors extensively utilize a commercial light sensor called a multi-pixel photon counter (MPPC) for the light collection in the scintillator-based detectors.

What follows from here is a description of the MPPC technology used in T2K. Next is a description of INGRID and its purpose at ND280. This is followed by a general description primary off-axis, magnetized detector. This subsection is finished with descriptions of two subdetectors in the off axis detector. The first and second being the pi-zero detector (PØD) and time projection chamber (TPC), respectively.

From here on unless specified, INGRID will refer only to the on-axis ND and ND280 will refer only to off-axis ND.

1.2.2.1 Multi-pixel photon counter (MPPC)

While the reliable photo-multiplier tube (PMT) technology was used in previous scintillator-based detectors, T2K needed a different technology to work in the strong magnetic field environment. T2K selected a commercially available silicon photomultiplier sensor developed

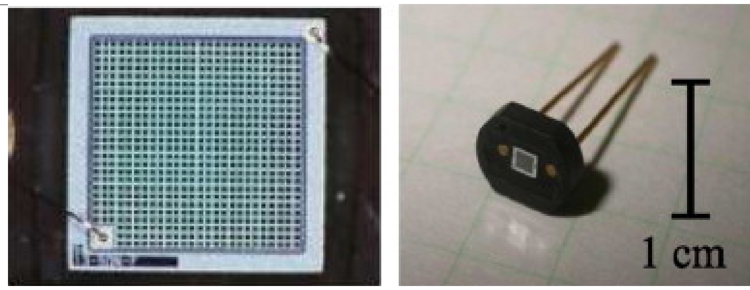

Figure 1.18: Photographs of the specially designed MPPC used in T2K. A magnified face view is shown on the left with an entire unit shown on the right [1].

by the Hamamatsu corporation called a MPPC. A MPPC is a compact device containing many sensitive avalanche photodiode pixels that act as Geiger micro-counters. They are well matched with the spectral emission of wavelength-shifting (WLS) fibers used to collect the scintillator light in ND280 and operate in a strong magnetic field environment. T2K utilizes specialized 667-pixel MPPCs with an effective area of 1.3 mm $\times$ 1.3 mm as shown in Figure 1.18 on page 33.

1.2.2.2 On-Axis Detector

The on-axis near detector called the Interactive Neutrino Grid (INGRID) is a tracking scintillator detector designed to directly measure the neutrino beam profile. As shown in Figure 1.17 on page 32, it is a cross grid of tracking modules centered at the designed neutrino beam center ($\theta = 0$). Each module consists of alternating layers of iron plates and scintillator bars except for the two most downstream scintillating layers which lack iron plates. To monitor the beam asymmetry, two separate modules are placed off the grid axis.

Each scintillating bar consists of scintillator-doped polystyrene which emits light when a charged particle deposits energy in the media. Each bar contains a single wavelength-shifting (WLS) fiber to collect and shift the light to a different energy. The light is collected at a single MPPC device and converted into an electrical signal. In order to enhance the collection efficiency, a reflective TiO_2 doped polystyrene shell surrounds each bar. Bars

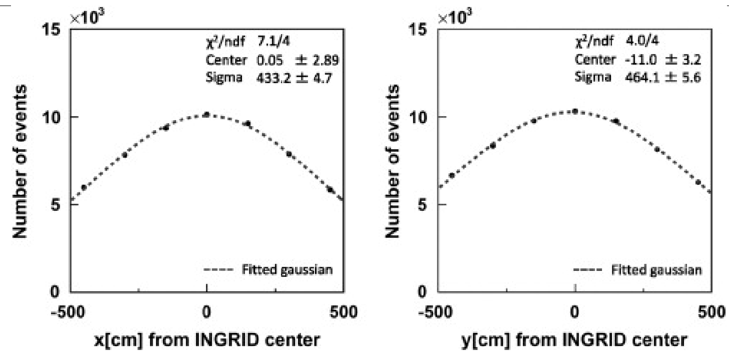

Figure 1.19: A beam profile taken with INGRID in April 2010 shows the Gaussian nature of the beam. The errors on the data points are about 1%. [2]

are assembled into planes to provide tracking capabilities. Veto planes also surround each module to prevent false signals to trigger.

INGRID is continually monitored to ensure the neutrino beam center is properly aligned at its designed center. Diagnostic plots such as Figure 1.19 on page 34 are collected on a monthly basis to ensure that the neutrino flux at Super-Kamiokande (SK) is consistent with T2K's design. A history of the beam profile and event rate on INGRID between January 2010 and October 2016 is shown in Figure 1.20 on page 35.

1.2.2.3 Off-Axis Detector Summary

The primary near detector for T2K, ND280, is an off-axis, magnetized tracking detector. It is a collection of different detector technologies designed to facilitate three measurement goals:

1. ν_μ flux at SK,
2. Irreducible ν_e background flux at SK, and
3. ν_μ interaction backgrounds and cross sections for the $\nu_\mu \rightarrow \nu_e$ search.

ND280 consists of the pi-zero detector (PØD), the tracker region consisting of a fine grain detector (FGD) and time projection chamber (TPC), an electromagnetic calorimeter (ECal), and side muon range detector (SMRD). The ND280 subdetectors are instrumented inside

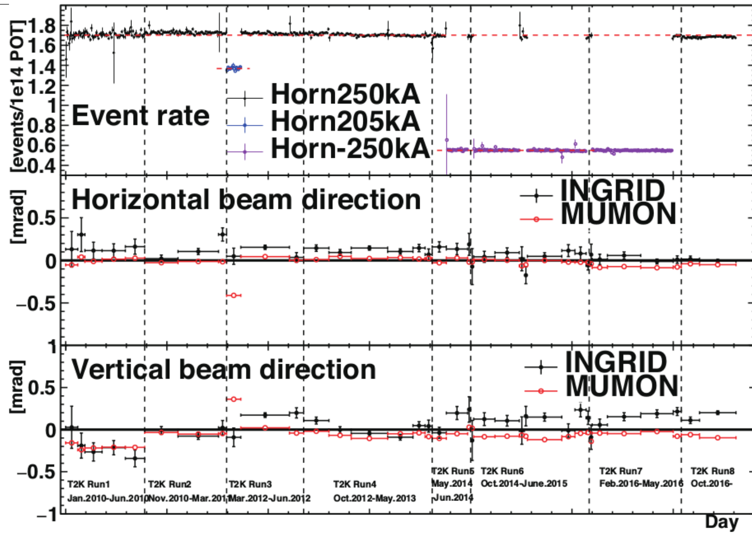

Figure 1.20: INGRID interaction event rate and beam profiles are shown. The top panel shows the event rate for the three different horn currents. The middle and bottom panels show the horizontal and vertical beam directions with respect to the beam center, respectively. A deviation of 1 mrad corresponds to a little under 30 cm. The error bars shown are the statistical errors on the mean.

the recycled UA1/NOMAD magnet with the SMRD in the magnetic field return yoke itself. All but the FGD is instrumented with the same scintillating-bar bar technology collected by MPPCs. A schematic of the different detector components of ND280 is shown in Figure 1.21 on page 36.

The focus of this thesis are the PØD and the TPC since they are the primary subdetectors used in the analysis. The PØD serves as a massive target for the incident neutrino beam and the TPC serves to measure the charge and momentum of the outgoing particles.

The ND280 magnetic field is generated using electrical current fed through solenoid coils to generate a dipole field of strength 0.2 T[10] in the x direction. The field is highly uniform near the center of the detector which is where the majority of the TPC system is located. However, it has significant deviations from 0.2 T near the solenoid edges. In order to fully understand the field inside ND280, a precise 3D model was generated using a machine

[10]This is a powerful magnetic field. According to the The US/UK World Magnetic Model for 2015-2020, the magnetic field strength on the surface of the Earth is about 0.294385 Gauss or 2.94385×10^{-5} T. So the field inside ND280 is about 6800 times more forceful than the Earth's influence [12].

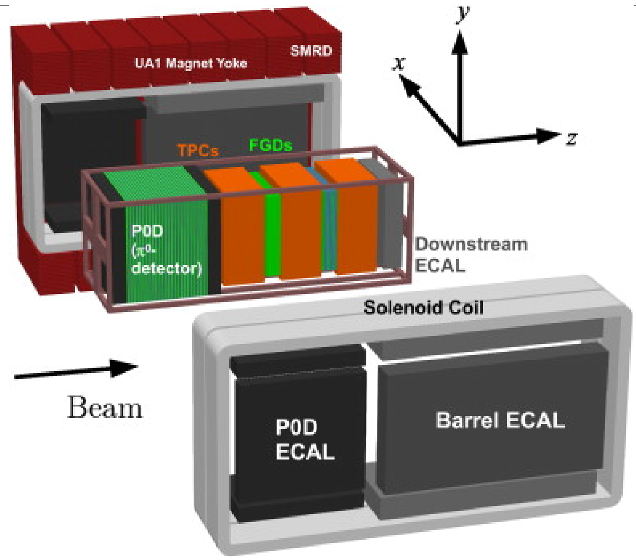

Figure 1.21: An exploded view of the ND280 off-axis detector. The magnetic field is generated from the Solenoid Coil via an electrical current which produces a dipole magnetic field of strength 0.2 T. The field is designed to return to the Magnetic Yoke.

controlled Hall probe. The operating field strength during the mapping process was 0.07 T due to power restrictions at the time. The model was then compared with measurements in the TPC region as shown in Figure 1.22 on page 37. After scaling the model to the nominal operating strength of 0.2 T, a fractional uncertainty of 10^{-3} or uncertainty of 2 Gauss in each direction was obtained.

The ND280 magnetic field permits the measurements of particle charge and momentum. A particle of charge q, rest mass m_0, and velocity $\mathbf{v}$ under the influence of an external electric and magnetic fields, $\mathbf{E}$ and $\mathbf{B}$, respectively, experiences a force $\mathbf{F}$ given by the Lorentz force equation

$$\mathbf{F} = q\left(\mathbf{E} + \mathbf{v} \times \mathbf{B}\right). \tag{1.49}$$

Assuming for now that there is no external electric field, the force on the particle is

$$\mathbf{F} = q\mathbf{v} \times \mathbf{B}, \tag{1.50}$$

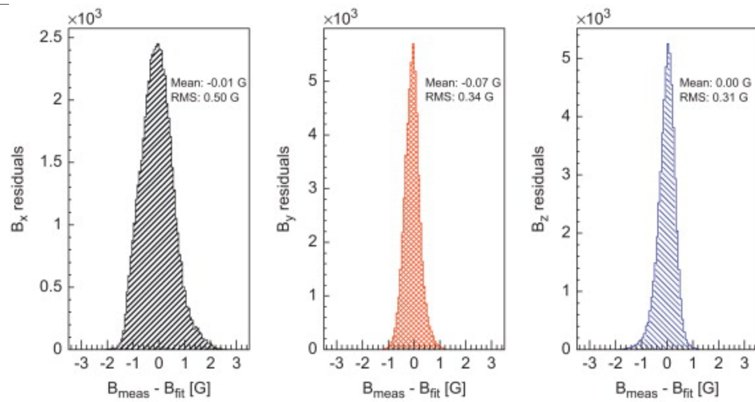

Figure 1.22: Each of the magnetic field components (x, y and z, respectively) are compared between a fit of the data and the actual measurements near the center of ND280. The systematic uncertainty on the field is extracted from the RMS of the mapping [1].

which is both orthogonal to $\mathbf{v}$ and $\mathbf{B}$. Since the mechanical work on a particle in a magnetic field is zero, the particle's energy is unchanged ($|\mathbf{v}| = v =$ constant). Newton's Second Law allows us to rewrite the force as an change in momentum $\mathbf{P}$

$$\begin{aligned}\mathbf{F} &= \frac{d\mathbf{P}}{dt} \\ &= \frac{d}{dt}\left(\gamma(v)m_0\mathbf{v}\right) \\ &= m_0\mathbf{v}\left(\frac{d\gamma(v)}{dt}\right) + \gamma(v)m_0\left(\frac{d\mathbf{v}}{dt}\right) \\ &= m_0\mathbf{v}\left(\frac{d\gamma(v)}{dv}\right)\cancelto{0}{\left(\frac{dv}{dt}\right)} + \gamma(v)m_0\mathbf{a} \\ &= \gamma(v)m_0\mathbf{a},\end{aligned} \tag{1.51}$$

where $\mathbf{P} = \gamma(v)m_0\mathbf{v}$ is the relativistic momentum and $\gamma(v) = \left(1 - (v/c)^2\right)^{-1/2}$ is the Lorentz factor for relativistic particles. For uniform circular motion, the magnitude of the acceleration is given by

$$|\mathbf{a}| = v^2/R, \tag{1.52}$$

where R is the radius of curvature for the circle. Combining equation (**??**) and equation (**??**) with some algebra yields

$$R = \frac{\gamma(v) m_0 v}{q\,|\mathbf{B}| \sin\theta_{\mathbf{vB}}}, \tag{1.53}$$

where $\theta_{\mathbf{vB}}$ is the angle between $\mathbf{v}$ and $\mathbf{B}$. The numerator of equation (**??**) is recognized as the magnitude of the momentum $|\mathbf{P}|$. Some further rearrangement yields

$$|\mathbf{P}| = q\,|\mathbf{B}|\,R \sin\theta_{\mathbf{vB}}, \tag{1.54}$$

and thus measuring the direction and radius of curvature inside the field provides the charge and momentum, respectively, as desired.

1.2.2.4 Off Axis pi-zero detector (PØD)

The PØD is the primary detector used a neutrino target in this thesis. It is a plastic scintillator based tracking calorimeter inside the ND280 magnet region. It is designed to measure the neutral current (NC) process $\nu_\mu + N \to \nu_\mu + N + \pi^0 + X$ on water where N is a nucleus and X is any set of final state particles. NC π^0 was expected to be a significant background in the ν_e appearance search in the likelihood that $\theta_{13} \approx 0$. The PØD is a dynamic detector which can be filled or drained of water enabling the determination of water target (WT) cross sections.

A representation of the PØD is shown in Figure 1.23 on page 39. The active detector components are very similar to INGRID's design where scintillation light is captured by a WSF and counted by a MPPC. Each bar is triangular in shape as shown in Figure 1.24 on page 40. A plane of 134 horizontal and 129 vertical bar together to form a PØD module (PØDule) as shown in 1.23b. The PØD dimensions are $2.298 \times 2.468 \times 2.350\text{m}^3$, in XYZ respectively, with a total mass of ∼1900 kg of water and 3570 kg of other material. The total mass of the PØD is approximately 15,800 kg when the bags are full of water. PØDules are arranged into three primary regions. The water target (WT) region contains 26 PØDules interleaved between bags of water 2.8 cm thick when filled and 1.3 mm thick brass sheets designed to help contain π^0 decay photons. The last two regions are the upstream ECal

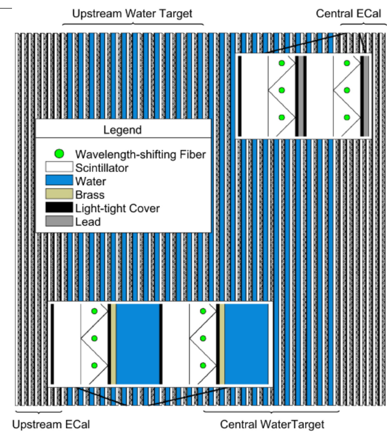

(a) Schematic of the PØD

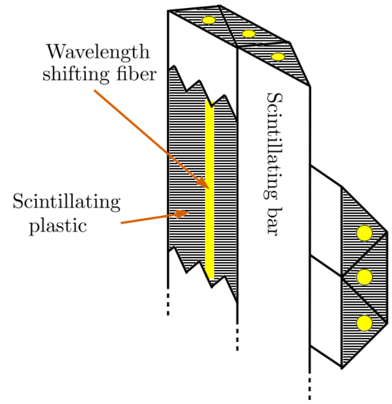

(b) Schematic of a PØD module

Figure 1.23: Schematics of the PØD. Left: insets detail the Water Target and ECal layers. Right: A view of a PØD module illustrating the orthogonal layout of the scintillating planes. Both: the neutrino beam is coming from the left.

Element	Symbol	Fraction [%]
Carbon	C	45.0
Oxygen	O	29.9
Copper	Cu	14.3
Hydrogen	H	8.0
Zinc	Zn	1.6
Chlorine	Cl	1.1
Titanium	Ti	0.1

Table 1.3: Elemental composition of PØD water target region. The table is sorted from top to bottom by fraction of mass. This table was originally produced in Reference [5]

(USECal) central ECal (CECal). Each ECal region contains 7 PØDules with steel sheets clad with lead between them [5]. An elemental composition of the WT is shown in Table 1.3 on page 39.

The readout electronics for the PØD is based on the Trip-T application specific integrated circuit (ASIC) shared among the SMRD, ECals, and INGRID. Signals from 64 MPPCs are routed to Trip-T front end boards (TFB) that each house 4 Trip-T ASICs. Each Trip-T collects the MPPC charge in 23 programmable integration cycles.

The TFB are readout to back-end electronics which control the TFBs and synchronize clocks. A total of six readout merger module (RMM) electronics receive TFB the data and

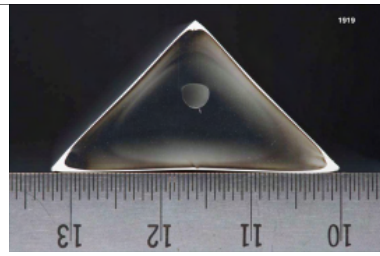

Figure 1.24: A cross section of a PØD scintillating bar. The base and height is 33 mm long and 17 mm high. The wavelength shifting fiber is inserted in the bored hole which is half-way between the base and tip.

control each TFB ASIC. RMM timing are synchronized with a cosmic trigger module and a slave clock module (SCM), of which both are synchronized with a master clock module from the beamline. Synchronizing the RMMs with the SCM allows for the Trip-T ASIC integration windows to match with the beam. The RMMs are responsible for distributing the TFB data to the data acquisition (DAQ) system for storage.

The ND280 DAQ consists of a MIDAS framework to monitor and control data collection. The primary client of the DAQ is to merge data and package it for long term storage. In parallel to it is the Global Slow Control (GSC) system which measures temperatures, voltages, and other physical quantities. Together the DAQ and GSC help scientists consistently produce high quality data and maintain the overall stability of the detector.

1.2.2.5 Off Axis Time Projection Chamber (TPC)

The ND280 TPC is designed to provide momenta measurements as discussed above, high resolution particle counting capabilities, and particle identification based on energy deposition. The latter most aspect is not utilized in this thesis. The TPC is divided into three volumes separated by the two FGD volumes. Each TPC volume ($2.3 \times 2.4 \times 1.0$ m^3) consists of an inner box that holds an argon-based gas and an outer box that holds an insulating CO_2 gas. The inner gas mixture is 3000 L of Ar:CF_4:iC_4H_{10} (95:3:2) gas. It was selected for its high speed, low diffusion, and good performance with the micromegas [1]. A simplified schematic of the TPC is shown in Figure 1.25 on page 41.

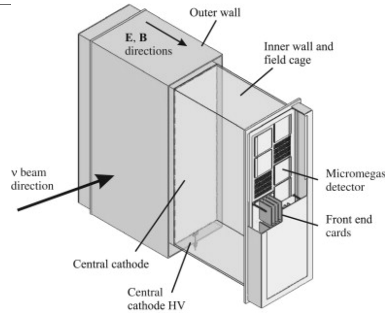

Figure 1.25: Cut-away drawing of a TPC volume in ND280 [1].

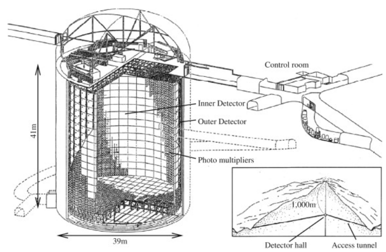

Figure 1.26: Diagram of the Super-Kamiokande detector consisting mainly of the inner and outer detector segments. The boundary between the two segments is cylindrical scaffolding used to mount photomultiplier tubes and optically isolate the segments.

As charged particles traverse the inner TPC volume, they create ionization electrons in the gas which drift towards readout planes away from a central cathode. The electron drift acceleration is rapid due to the strong 5 kV/cm electric field present. Drift electrons are multiplied and sampled by micromega detectors that line the sides of the TPC, providing nearly 3 m^2 of active surface coverage. Arrival times of the electrons provide timing information to give a full three dimensional portrait of the events.

1.2.3 Neutrino Far Detector: Super-Kamiokande

The Super-Kamioka neutrino detection experiment (Super-Kamiokande) is the dedicated far detector for the T2K experiment. Sitting at 295 km away from the neutrino source with a 1 km overburden, it is well designed to detect the elusive neutrino. Containing about 50 kt of pure water, is it lined with PMTs in both an inner and veto outer detector as shown in Figure 1.26 on page 41.

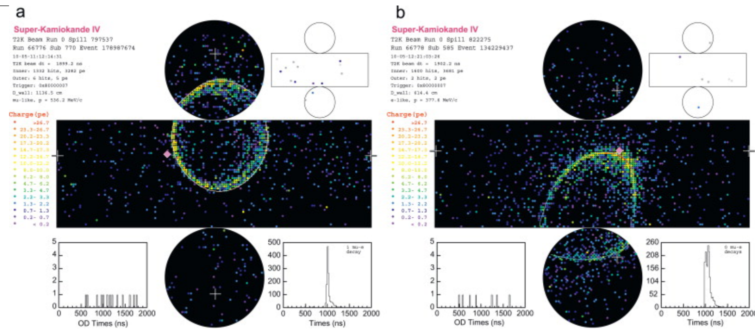

Figure 1.27: Representative T2K events in Super-Kamiokande for (a) a muon-like ring and (b) an electron-like ring. Both figures show Super-Kamiokande unrolled onto a plane with each colored point representing a PMT. The color of each PMT corresponds to the amount of charge collected. In upper right corner shows the same unrolled hit map for the veto outer detector. White crosses indicate the location of the reconstructed vertex. A solid diamond marks the location where a ray parallel to the beam would intersect the detector wall starting from the vertex.

When charged particles travel through the water, a Cherenkov radiation cone is produced. The sharpness of the cone edge is an unique ID for the particle species that produced it. An electron produces a fuzzy edge since it experiences many large multi-scatters off the water molecules. A muon on the other hand produces a sharp edge since it is much more massive and less perturbed by the molecules. Both types of events are shown in Figure 1.27 on page 42. By determining the particle that produced it and isolating the event during the T2K beam, the neutrino flavor is deduced.

While events from SK are not used in this analysis, the goal is to try to improve T2K's sensitivity to the currently unknown oscillation parameters.

1.2.3.1 Oscillation Analysis

The number of reconstructed neutrino events of flavor α observed at SK is sum of all true charged current (CC) events $S^{\mathrm{FD}}_{\nu_\alpha}$ and backgrounds B

$$N_{\nu_\alpha} = S_{\nu_\alpha} + B$$

where

$$S_{\nu_\alpha} = \sum_{i=1}^{M} \left\{ \sum_{\lambda=e,\mu,\tau} \left[\mathcal{P}_{\nu_\lambda \to \nu_\alpha}\left(E_{\nu,i};\vec{o}\right)\right] \times \sum_{t} \left[\sigma^t_{\nu_\alpha}\left(E_{\nu,i}\right) \ \cdot\ t_N\right] \right.$$
$$\left. \times \Phi_{\nu_\alpha}\left(E_{\nu,i}\right) \times \epsilon\left(p_\alpha, \theta_\alpha\right) \right\},$$

Chapter 2

BANFF Likelihood

The BANFF likelihood maximization procedure is a binned likelihood maximization of the ND280 data. In a ND280 and Super-Kamiokande (SK) joint fit, the measurements from both detectors are considered along with their respective nuisance parameters. This approach is more computationally expensive compared to the Markov Chain Monte Carlo analysis (MaCh3) which will not be explained here. The BANFF likelihood maximization, hitherto referred to as the "BANFF-fit", includes nuisance parameters that affect the measurement of the oscillation parameters, but are not physics goals of the T2K experiment. The BANFF-fit parameters and their respective covariances are then used as inputs in the oscillation analysis. This "divide-and-conquer" approach allows for more rapidly completed studies on the effects of model parameters and biases present. Also this approach should provide the same result with a joint ND280 and SK analysis as is performed in MaCh3. However, information encoded in the ND280 measurements for shared nuisance parameters like the neutrino flux is inevitably lost in the BANFF-fit.

The modern BANFF-fit likelihood is described in detail in TN-220 [17]. It uses a frequentist approach to find the best nuisance parameter set to maximize a binned likelihood. Subsequent updates to the BANFF analysis [**?**,9,18] increase the sample sizes and systematic parameterizations.

2.0.1 Motivation

Curve fitting is commonly found in the particle physics community literature due to the need to compare two models or constrain unknown model parameters using one or more histograms. For the first case, this involves two competing models, H_0 and H_1, in order to establish if the data supports new Physics (H_1) not predicted in the Standard Model (H_0). The second case finds the "best" set of the model predictions, θ, that match the data as is the case for the BANFF-fit. In both cases, chi-squared tests are performed to provide goodness of fit, parameter estimation (also referred to as "best fit parameters"), and error/confidence estimation.

2.0.2 Introduction to Conditional PDFs and Likelihoods

Consider the problem of extracting physics parameters $\vec{y}$ given some data vector $\vec{N}$. The conditional probability density function (PDF) $\mathcal{P}$ to measure these parameters is given as

$$\mathcal{P}\left(\vec{y}\middle|\vec{N}\right) = \frac{\mathcal{L}\left(\vec{N}\middle|\vec{y}\right)\mathcal{P}\left(\vec{y}\right)}{\int \mathcal{L}\left(\vec{N}\middle|\vec{x}\right)\mathcal{P}\left(\vec{x}\right)d\vec{x}}, \tag{2.1}$$

where anything right of a vertical line represents a condition on the probability, $\mathcal{L}\left(\vec{N}\middle|\vec{y}\right)$ is the likelihood of the model with parameters $\vec{y}$, $\mathcal{P}\left(\vec{y}\right)$ is the probability for the model, and the denominator is the normalization over all possible constraints on the observations. A frequentist interpretation of a PDF is a proportion of outcomes of repeated trials or experiments. A likelihood function is an expression of the probability of observing data as a function of the model parameters in their appropriate ranges.

One arrives at (2.1) by using the definition of compound probabilities

$$\mathcal{P}\left(A,B\right) = \mathcal{P}\left(B\left|A\right.\right)\mathcal{P}\left(A\right) \tag{2.2}$$

to evaluate $\mathcal{P}\left(\vec{y}\middle|\vec{N}\right)$ as

$$\mathcal{P}\left(\underbrace{\vec{y}}_{B}\middle|\underbrace{\vec{N}}_{A}\right)=\frac{\mathcal{P}\left(\vec{N},\vec{y}\right)}{\mathcal{P}\left(\vec{N}\right)} \tag{2.3}$$

with the denominator here is recognized as the normalization of the PDF. The compound PDF $\mathcal{P}\left(\vec{N},\vec{y}\right)$ can expanded using Bayes' theorem which states

$$\mathcal{P}\left(A\,|B\,\right)\mathcal{P}\left(B\right)=\mathcal{P}\left(B\,|A\,\right)\mathcal{P}\left(A\right), \tag{2.4}$$

and combined with (2.2) yielding

$$\mathcal{P}\left(\underbrace{\vec{N}}_{A},\underbrace{\vec{y}}_{B}\right)=\mathcal{P}\left(\vec{N}\middle|\vec{y}\right)\times\mathcal{P}\left(\vec{y}\right), \tag{2.5}$$

where the PDFs to the left and right of the $\times$ operator are recognized as the likelihoods and priors, respectively. Combining resulting in (2.3) and (2.5) reproduces the original expression of (2.1).

2.0.3 BANFF Fit Test Statistic

For the BANFF fit, one considers the problem of trying to maximize the agreement between measured and predicted data histograms. This is equivalent to maximizing a binned likelihood function $\mathcal{L}$ of the data given the a set of parameters that predict the measured rate. The use of likelihood functions in fits to histogram is explained further in reference [8] and the PDG review on Statistics. By invoking Wilks' theorem, also known as the likelihood ratio theorem, the likelihood maximization procedure is converted into a minimization problem involving a test statistic denoted as a chi-squared. Below is an explanation of the BANFF test statistic, $\Delta\chi^2$, and its systematic model terms.

Consider many binned samples that select different charged current topologies. A convenient choice of observables for all the samples are the outgoing charged lepton l momentum P_l and angle $\cos\theta_l$ as measured in ND280. Much of this is also documented in TN-220 [17] where additional details can be found. For each $(P_l, \cos\theta_l)$ analysis bin $i = 1, 2, \ldots, M-1, M$, the likelihood is given by

$$\mathcal{L}\left(\vec{N}^d \middle| \vec{N}^p\right) = \left(\prod_{i=1}^{M} \left(\vec{N}_i^p\right)^{\vec{N}_i^d} \frac{e^{-\vec{N}_i^p}}{\vec{N}_i^d!}\right) \tag{2.6}$$

where $\vec{N}_i^d$ is the number of observed data events in the ith bin and $\vec{N}_i^p$ is the number of predicted events as a function of nuisance parameters in the ith bin. One recognizes the likelihood function in (2.6) as a product of Poisson distributions with each corresponding to bins $i = 1, 2, \ldots, M-1, M$. The sets of dependent nuisance parameters, also sometimes called systematics, that affect the predicted event rate are

- cross section physics models, labeled as “xsec”,
- neutrino flux, and
- detector biases and inefficiencies.

Given these three sets of systematics, the number of predicted CC events from any neutrino flavor ν_l at ND280 is calculated using the general formula

$$N_{\nu_l} = \underbrace{\Phi_{\nu_l}}_{\text{Flux}} \left[\sum_t \underbrace{\left(\sigma_{\nu_l}^t M_t\right)}_{\text{Interactions}}\right] \underbrace{\epsilon_{\nu_l}}_{\text{Efficiency}}\ , \tag{2.7}$$

where Φ_{ν_l} is the flux of l flavor neutrinos, $\sigma_{\nu_l}^t$ is the cross section of the interaction for neutrino flavor l on target t, M_t is the number of t targets, and ϵ_{ν_l} is the total efficiency to reconstruct and properly identify the event as ν_lCC interactions. Since the cross section is a measure of interaction probability in units of area, multiplication of M_t represents the effective cross sectional area of material t in the detector. Each term in (2.7) is modeled carefully and the efficiency term is estimated using Monte Carlo (MC) simulations and control samples. The number of predicted events from the MC for a given analysis bin i is given by

$$\vec{N}_i^p\left(\vec{b},\vec{x},\vec{d}\right) = w_i^{\text{POT}}\left(\vec{d}\right)_i^{\text{Det}}\sum_{j=1}^{N_i^{\text{MC}}}\left[\sum_{k=1}^{N^{\text{Flux}}}\left(\delta_{j,k}^{\text{Flux}}\left(\vec{b}\right)_k^{\text{Flux}}\right)\prod_{l=1}^{N^{\text{xSyst}}} w_{j,l}\left(\left(\vec{x}\right)_l^{\text{xsec}}\right)\right]. \tag{2.8}$$

Here w_i^{POT} is the protons on target (POT) weight for the ith analysis which normalizes the MC statistics to expected data statistics. To account for the detector inefficiencies, the $\left(\vec{d}\right)_i^{\text{Det}}$ parameters are normalization parameters that vary the total number of predicted events in the ith bin. Each $\left(\vec{d}\right)_i^{\text{Det}}$ is determined prior to the fit by surveying over a large number of toy experiments with the detector systematics varied in each. The sum over $j = 1, 2, \ldots, N_i^{\text{MC}} - 1, N_i^{\text{MC}}$ considers the contribution of all MC events in the ith analysis bin. The $\left(\vec{b}\right)_k^{\text{Flux}}$ parameters, out of a total of N^{Flux}, are flux normalization systematics for each flux bin. Since the flux bins are categorized not only by neutrino energy, but also by flavor and horn current, the $\delta_{j,k}^{\text{Flux}}$ term in the sum over k selects the correct flux bin. The parameters $w_{j,l}$ are pre-calculated weights as a function for the lth cross section model, $(\vec{x})_l^{\text{xsec}}$, with a total of N^{xSyst} cross section model terms. Different t target materials have separate cross section parameters. Also the number of targets M_t can vary via detector systematics.

Using the likelihood ratio test theorem, a test statistic is defined as taking -2 times the natural logarithm of the ratio of predicted to observed likelihoods

$$\Delta\chi^2_{\text{LLR}} = -2\log\frac{\mathcal{L}\left(\vec{N}^d\middle|\vec{N}^p\right)}{\mathcal{L}\left(\vec{N}^d\middle|\vec{N}^d\right)}, \tag{2.9}$$

where this test statistic $\Delta\chi^2_{\text{LLR}}$ obeys a true chi-squared distribution for asymptotically large statistics and the likelihood functions are of the form (2.6). The denominator in (2.9) is the MC predicted probability which assumes the best maximum likelihood estimate is the number of observed events. Penalty terms from the cross section, flux, and detector systematics are included in order to prevent overfitting of the data. The new test statistic for all of ND280, $\Delta\chi^2_{\text{ND280}}$, is given by

$$
\begin{aligned}
\Delta\chi^2_{\mathrm{ND280}} &= \Delta\chi^2_{\mathrm{LLR}} + \Delta\chi^2_{\mathrm{xsec}} + \Delta\chi^2_{\mathrm{Flux}} + \Delta\chi^2_{\mathrm{Det}} \\
&\quad - 2\left(\log\frac{\mathcal{L}\left(\vec{N}^d \middle| \vec{N}^p\right)}{\mathcal{L}\left(\vec{N}^d \middle| \vec{N}^d\right)} + \log\underbrace{\pi\left(\vec{x}\right)}_{\mathrm{xsec}} + \log\underbrace{\pi\left(\vec{b}\right)}_{\mathrm{Flux}} + \log\underbrace{\pi\left(\vec{d}\right)}_{\mathrm{Det}}\right),
\end{aligned}
\tag{2.10}
$$

where each of the PDFs $\pi\left(\vec{y} = \vec{x}, \vec{b}, \vec{d}\right)$ are assumed multivariate normal distributions

$$
\pi(\vec{y}) = C_y e^{\left(-\frac{1}{2}\Delta\vec{y}\ \cdot\ V_y^{-1}\ \cdot\ \Delta\vec{y}^T\right)},
\tag{2.11}
$$

$\Delta\vec{y}$ is a vector with the difference between the current/explored and nominal set of vector parameters $\vec{y}$, T corresponds to the transpose operator, and the normalization is given by

$$
C_y = \left((2\pi)^{k_y} \det\left(V_y\right)\right)^{-\frac{1}{2}}
\tag{2.12}
$$

with V_y being the covariance matrix for a vector $\vec{y}$ with k_y rows. The expanded form of the test statistic $\Delta\chi^2_{\mathrm{ND280}}$ is given by

$$
\begin{aligned}
\Delta\chi^2_{\mathrm{ND280}} &= 2\sum_{i=1}^{M}\left[\vec{N}_i^p - \vec{N}_i^d + \vec{N}_i^d \log\left(\frac{\vec{N}_i^d}{\vec{N}_i^p}\right)\right] \\
&\quad + \Delta\vec{x}\ \cdot\ \left(V_x^{-1}\right)\ \cdot\ \Delta\vec{x}^T + \Delta\vec{b}\ \cdot\ \left(V_b^{-1}\right)\ \cdot\ \Delta\vec{b}^T + \Delta\vec{d}\ \cdot\ \left(V_d^{-1}\right)\ \cdot\ \Delta\vec{d}^T
\end{aligned}
\tag{2.13}
$$

where the " $\cdot$ " is the matrix multiplication operator. It must be stated that the test statistic (2.13) purposefully *excludes normalization terms*. Once the global minimum of the test statistic is found, the postfit covariance matrix V is calculated as the inverse of the Hessian matrix H

$$
V_{i,j}\left(\hat{\vec{y}}\right) = \left(H_{i,j}\right)^{-1} = \left(\frac{\partial^2}{\partial y_i \partial y_j}\left(\Delta\chi^2_{\mathrm{ND280}}\right)\Bigg|_{\vec{y}=\hat{\vec{y}}}\right)^{-1}
\tag{2.14}
$$

where $y_i, y_j \in \vec{y}$ and $\hat{\vec{y}}$ is the maximum likelihood estimate for the parameters $\vec{y}$.

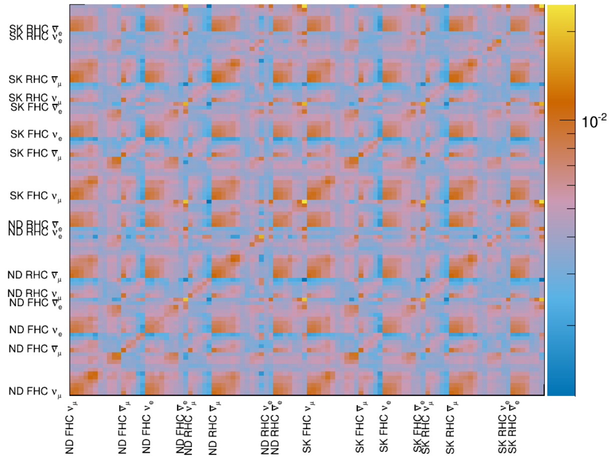

Figure 2.1: BANFF pre-fit flux covariance matrix shown with respective detector, horn current, and neutrino flavor.

2.0.3.1 Flux, Cross Section, and Detector Systematics

Below is a description for each of the systematics in the BANFF likelihood and test statistic penalty terms. First is a description of flux, followed by the cross section, and finally the detector systematics.

Flux: The flux weight is binned as a function of neutrino energy, horn current/polarity (FHC and RHC), and neutrino flavor (ν_μ, $\overline{\nu}_\mu$, ν_e, and $\overline{\nu}_e$). There are 50 ND280 and 50 SK parameters with an associated covariance matrix as shown in Figure 2.1. The binning and covariance matrix is provided by the T2K flux group prior to the BANFF analysis. Each flux bin is assigned a normalization parameter with initial value of one (1) for all events in that neutrino energy bin. A value of 1.1 indicates that any event in that energy bin has an additional weight of 1.1, or 10% increase in events. An example of the flux normalizations and uncertainties used in the 2017 analysis are shown in Figure 2.2.

Cross Section: There are a number of cross section model systematics implemented in BANFF to account for the uncertainties in cross section measurements. The cross section models used in this analysis are the 2017 Neutrino Interactions Working Group (NIWG) parameterization, which is a canonical set of parameters and covariance matrix shared among all analyses in T2K. A technical description of the 2017 parameterization is given in TN-

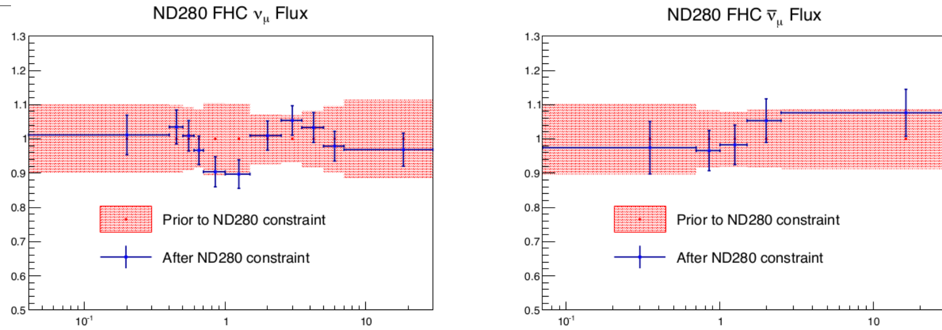

Figure 2.2: BANFF ND280 flux ν_μ and $\overline{\nu}_\mu$ binning parameters from T2K-TN-324 data post-fit results. The uncertainties are extracted from the pre-fit and post-fit covariance matrices.

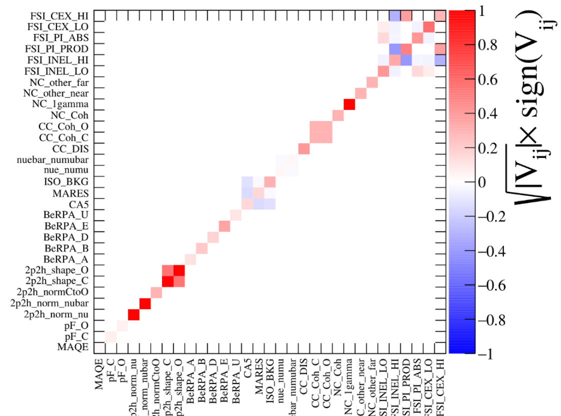

Figure 2.3: Cross section parameters pre-fit correlation matrix from the 2017 BANFF analysis.

315 [10] and TN-307 [22]. There are a total of 25 cross section parameters for interactions like meson exchange current that affect the shape and normalization of the cross section. The cross section correlation matrix is shown in Figure 2.3 [**?**].

Detector Systematic Errors: Detector systematics are implemented in BANFF to account for uncertainties in detector efficiencies. Since neutrino interaction events can migrate from sample-to-sample, bin-to-bin, or both depending on the relevant systematics, numerous toy experiments are performed by varying parameters that model known detector systematics.

After many toy experiments, a covariance matrix among the bins is constructed considering correlations and statistical errors. This detector covariance matrix is fractional to be consistent with the definitions for the flux and cross section covariance matrices. The detector covariance matrix, σ^2_{Det}, between bins x and y given explicitly as

$$\sigma^2_{\mathrm{Det}}(x,y) = \frac{1}{x_{\mathrm{Nom}}}\frac{1}{y_{\mathrm{Nom}}}\left(\sigma^2_{\mathrm{Cov}}(x,y) + \sigma^2_{\mathrm{Stat}}(x,y)\right), \tag{2.15}$$

where "Nom", "Cov", and "Stat" refer to the nominal MC prediction, covariance, and statistical uncertainties for bins x and y, respectively. The nominal bin expectation for bin x is

$$x_{\mathrm{Nom}} = \sum_{k=1}^{N_x^{\mathrm{MC}}} w_k, \tag{2.16}$$

where N_x^{MC} being the number of predicted MC events in the bin and w_k being the product of all the weights applied to the kth event (see (2.8) for all possible weights). The covariance and statistical terms are given by

$$\begin{aligned} \sigma^2_{\mathrm{Cov}}(x,y) &= \frac{1}{N_{\mathrm{Toy}}}\sum_{t=1}^{N_{\mathrm{Toy}}}(x_t - \overline{x})(y_t - \overline{y}) \\ \sigma^2_{\mathrm{Stat}}(x,y) &= \delta(x,y)\sum_{k=1}^{N_x^{\mathrm{MC}}} w_k^2, \end{aligned} \tag{2.17}$$

where N_{Toy} is the number of toy experiments, $\overline{x}$ is the mean of the all the toy experiments in bin x, and $\delta(x,y)$ is the Kronecker delta function. Additional uncertainties like fake data contributions are added to the covariance in quadrature.

While there could be one detector systematic normalization for each analysis bin, also called a observable normalization, a single one can be assigned to multiple analysis bins to reduce the number of fit parameters. This procedure requires careful consideration of the shared detector systematics among analysis bins. A considerable drawback to designing normalizations in this way is that not all detector systematics are Gaussian with respect to the observables $(P_l, \cos\theta_l)$, and so the covariance matrix may not be an accurate representation of the detector systematics.

Chapter 3

Systematic Uncertainties

Sources of systematic uncertainties, hitherto referred to as systematics, must be evaluated in order to understand their effect on any analysis. The BANFF fit utilizes a set of canonical systematics

3.0.1 Detector Systematic Uncertainties

All the detector systematics in BANFF are evaluated as either observable variations or weights. An observable variation affects the physical observables of selected events. The most important variation is the energy loss in the PØD of the outgoing muon in CC interactions.

3.0.1.1 Efficiency-like Systematics

Efficiency-like systematics are treated as weights to the MC predictions in order to evaluate the uncertainty the systematic has on an analysis. They are based on studies comparing data and MC predictions in well known control samples (CS). A CS is designed to provide a reliable measurement with minimal influence from other dependent and independent factors. An example of a well established CS is a collection of single, isolated cosmic ray (muon) tracks to measure the energy loss in a detector. In general, a CS may have different properties than the analysis sample like event topology. In particular the cosmic ray CS cannot account for efficiency effects of other tracks present. Therefore a model extrapolation is needed to map the CS to the analysis sample. The model used in psyche/BANFF is that the efficiency of the data and MC is the same in both analysis sample and CS

$$\epsilon_{\text{Data}}(o) = \left(\frac{\epsilon_{\text{Data}}(o)}{\epsilon_{\text{MC}}(o)}\right)_{\text{CS}} \epsilon_{\text{MC}}(o)$$

where $\epsilon_{\text{MC}}/\epsilon_{\text{Data}}$ denotes the mean efficiency of the MC/data as a function of some observable o. We need to update this model to account for statistical uncertainties in the CS. The updated model, with o dependence assumed, is now

$$\epsilon'_{\text{Data}} = \left(\frac{\epsilon_{\text{Data}} + x_{\text{Data}} \cdot \sigma_{\epsilon_{\text{Data}}}}{\epsilon_{\text{MC}} + x_{\text{MC}} \cdot \sigma_{\epsilon_{\text{MC}}}}\right)_{\text{CS}} \epsilon_{\text{MC}}$$

where $\sigma_{\epsilon_{\text{MC/Data}}}$ is the standard deviation of the efficiency of the MC/Data and x_{Data} and x_{MC} are different random, normally distributed numbers $\mathcal{N}\left(\mu = 0, \sigma^2 = 1\right)$.

$$w_{\text{eff}} = \frac{\epsilon'_{\text{Data}}}{\epsilon_{\text{MC}}}$$
$$w_{\text{ineff}} = \frac{1 - \epsilon'_{\text{Data}}}{1 - \epsilon_{\text{MC}}}$$

3.0.1.2 Observable Variation Systematics

$$o' = o_{\text{Nom}} + \overline{\Delta o} + x\sigma_{\Delta o},$$

where o' is the varied observable value, o_{Nom} is the nominal MC value, $\overline{\Delta o}$ is the average correction to the observable, $\sigma_{\Delta o}$ is the uncertainty on the correction, and x is a random number from $\mathcal{N}\left(\mu = 0, \sigma^2 = 1\right)$.

3.0.1.3 Normalization Systematics

Systematic effect	Treatment
TPC cluster eff.	efficiency
TPC tracking eff.	efficiency
TPC charge misassignment	efficiency
TPC momentum resol.	observable variation
TPC momentum scale	observable variation
B field distortion	observable variation
Pion secondary interactions	efficiency
Proton secondary interactions	efficiency
PØD energy loss scale	observable variation
PØD energy loss resol.	observable variation
PØD OOFV	efficiency
PØD track veto	efficiency

Table 3.1: [?]

$$w = w_0 \left(1 + x\sigma_w\right)$$

Chapter 4

PØD in BANFF Parameterization

4.0.1 PØD Samples Fit Binning

The PØD ND280 BANFF fit uses the samples described in **??**. The bin edges are tabulated below.

- FHC ν_μCC 1-Track bin edges:

  p [GeV/c]: 0, 0.3, 0.4, 0.5, 0.6, 0.7, 0.8, 1, 1.25, 1.5, 2, 3, 4, 5.5, 30

  $\cos\theta$: -1, 0.7, 0.8 , 0.88, 0.94, 0.96, 0.975, 0.99, 1

- FHC ν_μCC N-Tracks bin edges:

  p [GeV/c]: 0, 0.4, 0.5, 0.6, 0.7, 0.8, 1, 1.2, 1.5, 1.8, 2.2, 2.7, 3.5, 5, 10, 30

  $\cos\theta$: -1, 0.65, 0.77, 0.85, 0.9, 0.94, 0.97, 0.99, 1

- RHC $\overline{\nu}_\mu$CC 1-Track bin edges:

  p [GeV/c]: 0, 0.4, 0.5, 0.6, 0.7, 0.8, 1, 1.25, 1.5, 2, 3, 30

  $\cos\theta$: -1, 0.82, 0.87, 0.9, 0.93, 0.95, 0.97, 0.99, 1

- RHC $\overline{\nu}_\mu$CC N-Tracks bin edges:

  p [GeV/c]:0, 0.5, 0.9, 1.25, 1.6, 2, 3, 8, 30

$\cos\theta$: -1, 0.8, 0.89, 0.95, 0.97, 0.99, 1

- RHC ν_μCC 1-Track bin edges:

  p [GeV/c]: 0, 0.4, 0.6, 0.8, 1.1, 2, 10

  $\cos\theta$: -1, 0.78, 0.84, 0.89, 0.92, 0.95, 0.97, 0.98, 0.99, 1

- RHC ν_μCC N-Tracks bin edges:

  p [GeV/c]:0, 0.4, 0.6, 0.8, 1, 1.5, 2, 3, 10

  $\cos\theta$: -1, 0.7, 0.8, 0.85, 0.9, 0.94, 0.965, 0.98, 0.99, 1

4.0.1.1 Fit Binning Determination

The fit binning is designed to optimized to ensure at least 1 predicted Monte Carlo (MC) event in each bin when scaled to the collected data POT. The fit bins must also account for detector smearing effects. In order to mitigate smearing and event migration, the reconstructed kinematics were examined to their MC truth value using only correctly identified leptons in one-dimensional kinematic slices. Since the MC provides about 10× the data statistics, the statistical uncertainty for each bin should be negligible for high statistics regions. The kinematics are scanned across their full relevant spaces in order to understand the needed width for a fit bin. The first fit bin is always defined from the kinematic maximum.

For the momentum bins, the momentum resolution is compared to MC truth. The momentum resolution is defined as

$$R(r,t) = \frac{r-t}{t},$$

where r is the reconstructed momentum and t is the true value. The momentum was scanned in finite bin widths with the mean and standard deviation of the resolution R extracted. The mean and standard deviation are used as a proxy for the true bias and true resolution, respectively. In addition, a bootstrapping algorithm was employed to understand the accuracy

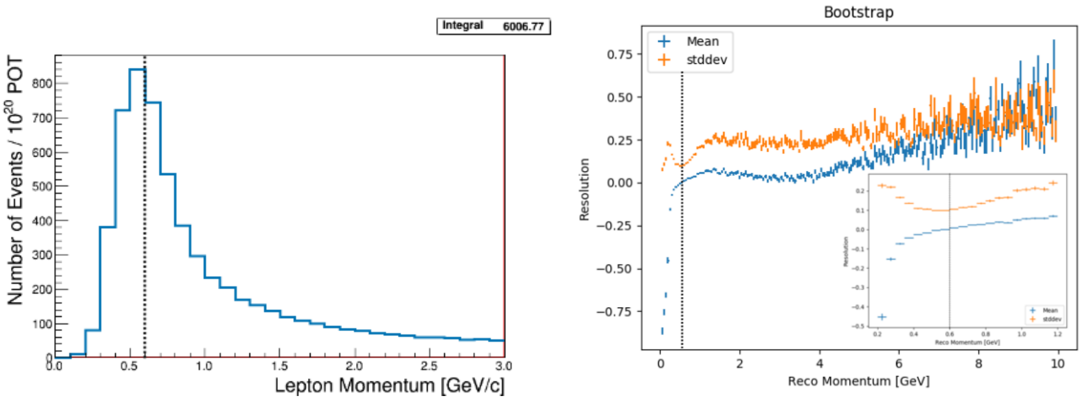

(a) Momentum event distribution

(b) Momentum resolution

Figure 4.1: The momentum event distribution and uncertainty for FHC ν_μCC 1-Track events is shown above. Only correctly identified muons are shown. (a) The number of events per unit momentum is scaled to 10^{20} POT which is the approximate scale for all the samples in this analysis. A dashed line indicates the maximum of the peak. (b) The resolution of the momentum measurement is shown for a wide region of momenta. In the inset is the resolution zoomed near the momentum distribution maximum. Like in (a), a dashed line shows the momentum maximum.

of the sample estimates. Bootstrapping in this context is sampling over all relevant values of true momentum and randomly replacing the values. For each scanned bin, at least 1000 bootstrapping sampling with replacement was performed. In the case of large variances in the bootstrapping samples, additional 10000 sampling with replacement were performed. The results for analyzing the FHC ν_μCC 1-Track selection is shown in Figure 4.1 on page 58.

The angle bins are treated in an almost identical manner. While the fit bins and physics parameterized in $\cos\theta$, the angle with respect to the z-axis, the detector smearing is a function of the angle θ. In addition, since the angle can be nearly zero for the most forward-going tracks, the resolution was not used to characterize the angular uncertainties. Instead, the difference between the true and reconstructed angle were analyzed as shown in . The mean and standard deviation were studied. Bootstrapping was again used to quantify the accuracy of the mean and standard deviation.

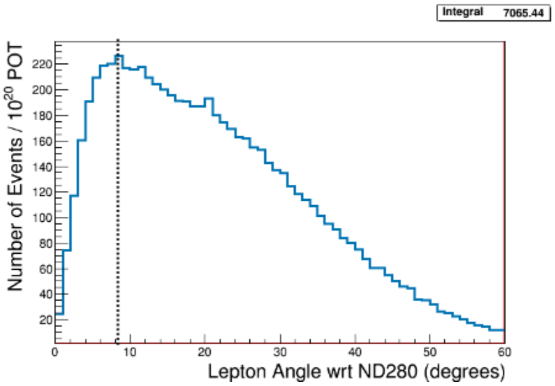

(a) Angular event distribution

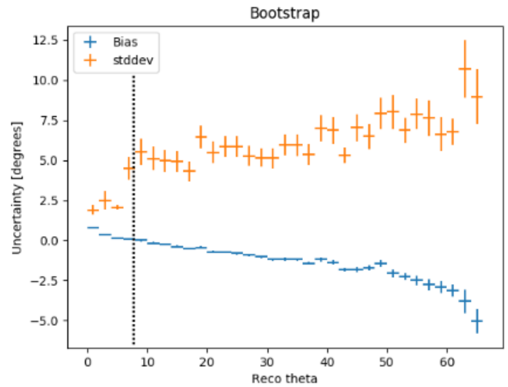

(b) Angular residuals

Figure 4.2: The angular event distribution and uncertainty for FHC ν_μCC 1-Track events is shown above. Only correctly identified muons are shown. (a) The number of angular events is scaled to 10^{20} POT which is the approximate scale for all the samples in this analysis. A dashed line indicates the maximum of the peak. (b) The residual of the angular measurement is shown up to where there are sufficient statistics. Like in (a), a dashed line shows the momentum maximum.

Bibliography

[1] K. Abe et al. The T2K Experiment. *Nucl. Instrum. Meth.*, A659:106–135, 2011. 25, 28, 29, 31, 33, 37, 40, 41

[2] K. Abe et al. Measurements of the T2K neutrino beam properties using the INGRID on-axis near detector. *Nucl. Instrum. Meth.*, A694:211 – 223, 2012. 32, 34

[3] K. Abe et al. Observation of Electron Neutrino Appearance in a Muon Neutrino Beam. *Phys. Rev. Lett.*, 112:061802, 2014. 26

[4] K. Abe et al. Search for CP Violation in Neutrino and Antineutrino Oscillations by the T2K Experiment with 2.2×10^{21} Protons on Target. *Phys. Rev. Lett.*, 121:171802, Oct 2018. 26

[5] K. Abe and Others. Measurement of ν_μ and $\overline{\nu}_\mu$ charged current inclusive cross sections and their ratio with the T2K off-axis near detector. *PHYSICAL REVIEW D*, 96(5), September 2017. 39

[6] C. Adams et al. The Long-Baseline Neutrino Experiment: Exploring Fundamental Symmetries of the Universe. 2013. arXiv:1307.7335. 4, 21, 25

[7] Jiro Arafune, Masafumi Koike, and Joe Sato. CP violation and matter effect in long baseline neutrino oscillation experiments. *Phys. Rev. D*, 56:3093–3099, Sep 1997. 24

[8] S. Baker and R. D. Cousins. Clarification of the use of Chi-Square and Likelihood Functions in Fits to Histograms. *Nucl. Instrum. Meth.*, A221:437–442, 1983. 46

[9] S. Bienstock et al. Assessing the effect of cross-section model uncertainties on the T2K oscillation analyses with simulated data studies using the BANFF, MaCh3, P-Theta and VALOR frameworks, May 2018. T2K-TN-331 v5. 44

[10] S. Bolognesi and Others. NIWG model and uncertainties for 2017 oscillation analysis, April 2017. T2K-TN-315 v5. 51

[11] J-PARC Center. What is J-PARC?, January 2019. https://j-parc.jp/researcher/en/about/what/index.html, Accessed on 26 January 2019. 27

[12] A. Chulliat and Others. The US/UK World Magnetic Model for 2015-2020. Technical report, National Geophysical Data Center, NOAA, 2015. 35

[13] A. de Gouvea et al. Working Group Report: Neutrinos. In *Proceedings, 2013 Community Summer Study on the Future of U.S. Particle Physics: Snowmass on the Mississippi*, 2013. arXiv:1310.4340. 21

[14] I. Esteban et al. Global analysis of three-flavour neutrino oscillations: synergies and tensions in the determination of θ_{23}, δ_{CP}, and the mass ordering. 2018. arXiv:1811.05487. 23

[15] A. Ferrero. The ND280 Near Detector of the T2K Experiment. *AIP Conference Proceedings*, 1189(1):77–82, 2009. 25

[16] S. Fukuda et al. The Super-Kamiokande detector. *Nuclear Instruments and Methods in Physics Research Section A: Accelerators, Spectrometers, Detectors and Associated Equipment*, 501(2):418 – 462, 2003. 25

[17] M. Hartz and Others. Constraining the Flux and Cross Section Models with Data from the ND280 Detector for the 2014/15 Oscillation Analysis, May 2015. T2K-TN-220 v4. 44, 46

[18] M. Hartz and Others. Constraining the Flux and Cross Section Models with Data from the ND280 Detector using FGD1 and FGD2 for the 2016 Joint Oscillation Analysis, June 2016. T2K-TN-230 v3. 44

[19] Susumu Igarashi. Recent Progress of J-PARC MR Beam Commissioning and Operation. In *Proceedings, 57th ICFA Advanced Beam Dynamics Workshop on High-Intensity and High-Brightness Hadron Beams (HB2016): Malmö, Sweden, July 3-8, 2016*, page MOAM6P60, 2016. 28

[20] C. Jarlskog. A Basis Independent Formulation of the Connection Between Quark Mass Matrices, CP Violation and Experiment,. *Z. Phys.*, C29:491–497, 1985. 22

[21] E. Komatsu and Others. Seven-year Wilkinson Microwave Anisotropy Probe (WMAP) Observations: Cosmological Interpretation. *Astrophys. J.*, 192:18, February 2011. 24

[22] K. Mahn and Others. Implementation of new cross section parameters for the 2017 oscillation analysis, 2017. T2K-TN-307. 51

[23] Z Maki, M. Nakagawa, and S. Sakata. Remarks on the Unified Model of Elementary Particles. *Progr. Theor. Exp. Phys.*, 28(5), 1962. 19

[24] B. Pontecorvo. Inverse Beta Processes and Nonconservation of Lepton Charge. *J. Exp. Theor. Phys.*, 28(5), 1957. 19

[25] P. K. Saha et al. Simulation, measurement, and mitigation of beam instability caused by the kicker impedance in the 3-GeV rapid cycling synchrotron at the Japan Proton Accelerator Research Complex. *Phys. Rev. Accel. Beams*, 21:024203, Feb 2018. 28

[26] Andrei D Sakharov. Violation of CP invariance, C asymmetry, and baryon asymmetry of the universe. *Soviet Physics Uspekhi*, 34(5):392, 1991. 25

[27] N. Schmitz. *Neutrinophysik*. Teubner, Stuttgart, 1997. 18

[28] T. Sekiguchi et al. Development and operational experience of magnetic horn system for T2K experiment. *Nuclear Instruments and Methods in Physics Research Section A: Accelerators, Spectrometers, Detectors and Associated Equipment*, 789:57 – 80, 2015. 29

[29] M. Tanabashi et al. The Review of Particle Physics. *Phys. Rev. D*, 98(030001), 2018. 19, 23

[30] Peter von Ballmoos. Antimatter in the Universe: constraints from gamma-ray astronomy. *Hyperfine Interactions*, 228(1):91–100, Oct 2014. 24

[31] Y. Yamazaki, editor. *Accelerator technical design report for high-intensity proton accelerator facility project, J-PARC*. Number 2002-013. Japan Atomic Energy Research Institute, 2003. 28

[32] Kai Zuber. *Neutrino Physics*. CRC Press, Boca Raton, FL., 2nd edition, 2012. 2, 13, 18